
Master Thesis in Mechanical Engineering

# Development of 3D computational models of biodegradable meshes

**Author**:
Hugo Borges Carneiro Espírito Santo

**Supervisor**:
Dr. Maria Elisabete Teixeira da Silva

**Co-Supervisors:**
Prof. Dr. António Augusto Fernandes
Dr. Rita Rynkevic

Master in Mechanical Engineering

April, 2022

**Acknowledgements**

O meu percurso académico culmina agora numa nota de agradecimentos que nunca fará jus à dimensão do significado que esta etapa teve para mim, muito menos à gratidão que sinto para com todos os que me apoiaram e aconselharam ao longo deste tempo. Mesmo assim, arrisco-me a enumerar essas identidades exemplares. Reconheço, acima de tudo, o financiamento garantido pelo FCT ao projeto SPINMESH-POCI-01-0145-FEDER-029232. Este trabalho contou com o apoio do FCT e do INEGI, pelo LAETA,nos projetos UIDB/50022/2020 e UIDP/50022/2020.

Aproveito, em primeiro lugar, para agradecer à minha orientadora, Doutora Maria Elisabete Teixeira da Silva que me guiou ao longo deste trabalho com profissionalismo e dedicação. Importa também referir os meus co-orientadores, a Doutora Rita Rynkevic e o Professor António Augusto Fernandes que me aconselharam no meu projeto. Da mesma forma, destaco a prontidão demonstrada pelo Professor Marco Parente durante este tempo, tendo contribuído eficazmente para a realização deste trabalho.

Agradeço a todos os membros da Faculdade de Engenharia da Universidade do Porto, do Instituto de Ciência e Inovação em Engenharia Mecânica e Engenharia Industrial e, em especial, do Laboratório de Desenvolvimento de Produtos e Serviços pela oportunidade de realizar esta tarefa num ambiente de interajuda e companheirismo.

Destaco o eterno obrigado à minha família, pais, irmão, avós e tios, pelos sucessivos votos de confiança que depositaram em mim ao longo do curso. Uma referência que personifica o maior dos amores e paciências.

Por fim, que se brinde à amizade. Nenhuma relação alguma vez será unilateral por isso as personagens principais jamais precisariam de ver o seu nome escrito aqui. Um bem haja aos que me viram entrar, aos omnipresentes e aos que agora saem comigo, a história recomeça todos os dias.

Hugo Espírito Santo

**Abstract**

Pelvic Organ Prolapse has been studied for years - as the consequent damage to vital organs harnesses the health of many women, leading to pain and discomfort - and deserves the greater focus during the current work. Given the fact that its occurrence is associated with the weakening of the pelvic floor muscles and ligaments, all the features of the pelvic cavity are addressed.

The reviewed literature is meant to serve as a guideline for understanding the causes, implications and possible solutions for this medical condition. Treatment techniques are split between conservative and surgical approaches, depending on the severity of the injury. The surgical treatment is supported by the implantation of meshes, meant to compensate for the compromised functioning of degraded natural tissues.

Even though these techniques have been perfected in the past, many solutions cannot deliver convincing or safe results. Improved production techniques and materials have been put into play in order to achieve more adequate solutions. Melt electrospinning writing is one of these techniques and poly $\epsilon$-caprolactone - a biodegradable polymer – a new material that has shown interesting results during uniaxial tensile tests developed on mesh prototypes. The current work relies on the data collected from those tests, in order to model the meshes' behaviour on ABAQUS® software.

Once these meshes are built superimposing several filaments of two distinct diameters measuring 160 and 240 micrometres, the last are also simulated in order to assess the best constitutive model to represent their stress-strain relationship – the Linear Elastic model is found to be the best option. This model is used in the mesh simulations thereafter so that the influence of the sectional area may be understood - the structure overall capacity of enduring higher loads increases with the sectional area.

A square-shaped and a cross-shaped geometries are modelled in order to see how the stress distributions change as a function of the design – it is verified that the meshes built with the 160 micrometres diameter filaments are the best option to match the vaginal tissue curve up to a 6% elongation and that the meshes built with the 240 micrometres diameter filaments and the Restorelle® commercial mesh show similar behaviours inside the comfort zone.

## Resumo

O Prolapso Pélvico tem sido alvo de sucessivos estudos ao longo dos últimos anos – dada a complexidade dos danos associada aos órgãos da cavidade pélvica, que levam a sensações de desconforto e dor por parte dos pacientes – e recebe especial atenção ao longo do presente trabalho. Uma vez que a ocorrência desta condição está relacionada com o enfraquecimento dos músculos do pavimento pélvico, assim como com os ligamentos da cavidade, a constituição deste é cuidadosamente estudada.

A bibliografia revista serve como base de compreensão das causas, implicações e possíveis soluções para este problema de saúde. As técnicas de tratamento dividem-se entre conservadoras e cirúrgicas, dependendo da gravidade da lesão. O tratamento cirúrgico é suportado pela implantação de malhas, destinadas a compensar o mau funcionamento dos tecidos degradados.

Apesar do facto destas técnicas terem vindo a ser aperfeiçoadas no passado, nem todas as soluções garantem resultados convincentes ou seguros. A necessidade de encontrar novos métodos de produção destas malhas, suportados por materiais inovadores, é evidente. A impressão 3D aparece como promissora, nomeadamente a técnica de *melt electrospinning*, assim como o *poly $\epsilon$-caprolactone* – um polímero biodegradável – que tem demonstrado resultados interessantes em ensaios de tração uniaxial aplicados a protótipos de malhas compostos pelo mesmo.

O presente trabalho assenta dos dados experimentais retirados dos mencionados ensaios, com o objetivo de simular o comportamento das malhas no programa ABAQUS®. Sendo estas malhas constituídas pela sobreposição de filamentos de diâmetros de 160 e 240 micrómetros, estes são também simulados de forma a encontrar o melhor modelo constitutivo para reproduzir a relação tensão-deformação registada nos ensaios – o modelo linear elástico apresenta-se como o mais apropriado. Este modelo é usado nas simulações das malhas com o objetivo de perceber a influência do valor da área de secção – a capacidade de suportar valores superiores de tensão aumenta com a área de secção.

Duas geometrias distintas, uma quadrada e outra cruzada, são modeladas de de forma a visualizar a influência do design nas distribuições de tensão ao longo das estruturas – verificando-se que as malhas constituídas por filamentos com diâmetro de 160 micrómetros são a melhor opção para reproduzir o comportamento do tecido vaginal até 6% de elongação e, por outro lado, que as malhas constituídas por filamentos com diâmetro de 240 micrómetros apresentam um comportamento similar ao das malhas comercialmente utilizadas da Restorelle® para toda a zona de comforto de deformação.

*'An intellectual says a simple thing in a hard way. An artist says a hard thing in a simple way."*

Charles Bukowski

# Contents

# List of Figures

# List of Tables

# Chapter 1
# Thesis Report

## 1.1 Introduction

The present work has been developed on behalf of the final Dissertation of the Integrated Master Degree in Mechanical Engineering from the Faculty of Engineering of the University of Porto with the purpose of developing 3D computational models for Pelvic Organ Prolapse-Repairing 3D-Printed Biodegradable Mesh Implants.

Pelvic organ prolapse (POP), as a consequence of the weakening of interior supportive structures such as muscles and ligaments, can lead to serious discomfort and even organ failure [2]. Surgical implants are, up to the date of the current work's writing, the most reliable solution for restoring the natural position of the uterus. However, past solutions were not completely successful once many patients experienced injuries and discomfort after the surgery [3]. The fact that these implants often lead to pain and bleeding is a serious concern inside the community [4]. Plus, a proper match between the properties of the implants and the ones of the biological tissues to be repaired may be another performance factor to consider.

Aiming at a better understanding of the properties of biodegradable mesh implants, a less harmful option for the host, simulations on the mechanical behaviour of filaments were firstly set into motion. Relying on previous experimental data collected from tensile tests, several constitutive models - for samples produced through melt electrospinning writing [5] - were tested so that the best fit could be found and used in the mesh simulations afterwards. Simulating different mesh geometries with accuracy (also in comparison to experimental data) would guarantee that the chosen model was indeed appropriate, enabling the creation of new geometries and, ultimately, a more adequate solution for the mesh implants themselves.

## 1.2 Background and Main Objectives

Previous research has been carried out by many authors on how to deal with pelvic health conditions [6]. Increased life expectancy due to healthcare

improvements is a key factor for the incidence of POP to keep rising in the future, hence the importance of properly understanding its fundamental causes. Given the fact that the impairment degree of the pelvic ligaments defines the severity of the condition, tracking the several prolapse stages stands as crucial. Many studies have also been published on those terms, resorting to in vitro experiments to evaluate the behaviour of the pelvic ligaments, vaginal tissue and *levator ani* [7]. The results obtained from these experiments were able to represent the real in vivo behaviour of the tissues [8], and represent the best reference for the extraction of such data.

Regarding potential solutions for POP treatment, biodegradable implants must be highlighted. Previous research [5] thoroughly dedicated to understand how feasible the combination of 3D printing and biodegradable polymers would be for the production of such implants. The main goal of the current work was, serving as a follow-up approach, to evaluate which constitutive models would present as the most adequate to simulate filament and mesh mechanical behaviour, in order to avoid unnecessary costs in the development and improvement of the biodegradable implants.

## 1.3 Dissertation Outline

Besides the present Thesis Report, the current work features six other chapters, enumerated and described below.

In Chapter 2, "Literature Review", a base context is presented for the Female Pelvic anatomy, Pelvic Organ Prolapse and related treatments, as well as the theory supporting the adequacy of PCL and Melt Electrospinning for implant manufacturing.

In Chapter 3, "Computational Modelling", a first approach to the stress distribution analysis is made, so as to the main constitutive models used for the simulations developed in ABAQUS®.

In Chapter 4, "Finite Element Simulations", a full characterization of the constitutive models is shown, before moving into the application of numerical simulations on filaments and meshes

In Chapter 5, "Results and Discussion", the outcome of the analyses is presented according to each model, analysing the results and comparing them to the experimental data.

In Chapter 6, "Conclusion", the final considerations regarding the current work are presented, along with the potential future work on the subject.

# Chapter 2
# Literature Review

## 2.1 Female Pelvis Anatomy

As a life supporting structure and the room of numerous vital organs, the female pelvis has been thoroughly and specifically studied in past years with the purpose of better understanding, predicting and solving potential health conditions related to degenerated tissues. Whereas the male pelvis shows a more balanced geometry, the wider outlet diameter and circular shape seen on the female anatomy, nevertheless crucial for head engagement and parturition, predisposes to subsequent pelvic floor weakness [9].

The encircling bony structure is composed by 2 innominate bones, or hip bones, which are fused to the sacrum posteriorly and to each other anteriorly at the pubic symphysis. Several protrusions and ledges constitute attachment sites for muscles, fascial layers and ligaments. One of these, assumed as of great importance, is the thin and triangular sacrospinous ligament which, connecting the ischial spines to the lateral margins of the sacrum and coccyx anteriorly to the sacrotuberous ligament, reinforces the ground support for the cavity's interior. The pelvis has 2 basins: the major pelvis and the minor pelvis. The abdominal viscera occupy the major pelvis; the minor pelvis is the narrower continuation of the major pelvis inferiorly. The inferior pelvic outlet is closed by the pelvic floor [9].

Inside the cavity, the uterosacral (USLs) and cardinal ligaments (CLs) provide apical support to the upper vagina and uterus [9]. It is the impairment of these tissues that compromises the stability of the whole region. Simulations of the mechanical properties of the pelvic tissues have been used in [8], with the intention of delivering pelvic implants capable of mimicking the behaviour of those tissues.

### 2.1.1 Bone Cavity

The pelvic girdle connects the vertebral column (axial skeleton) to the two femora (appendicular skeleton). Transmitting weight from the upper body to the lower limbs during locomotion and while standing, as well as supporting the weight of the upper body when seated or stationary are the main functions

of the pelvic girdle. Two deep articular depressions are found on the bony pelvis, the acetabula, which give room to the right and left femoral heads and form the corresponding hip joint. On the superior end, the bony pelvis also offers support to the vertebral column via the articulation between the top of the sacrum and the lumbar vertebrae [10].

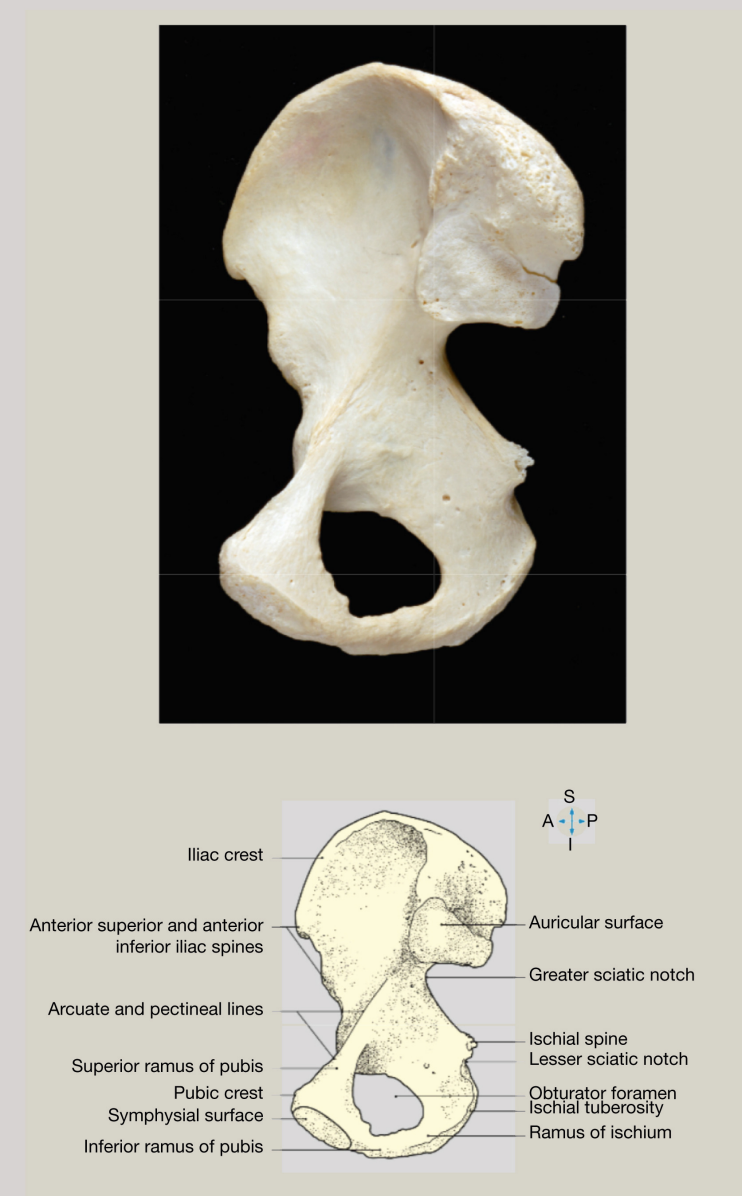


Figure 2.1: Right hip bone [10].

At each side of the hip bone - Figure 2.3 - stands the iliac crest which ends in the anterior superior iliac spine and posterior superior iliac spine, at its anterior and posterior extremities, respectively. Apart from the iliac crest, in the cavity also lie three other bones (the pubis, the ischium and the ilium) which compose the hip bone, merging at a Y-shaped epiphysis (the triradiate cartilage) at the acetabulum. The differentiation between the true and false

pelvis is given through the plane of the pelvic grim (or pelvic inlet), that shows a 60 degree inclination to the horizontal. Below the level of the pelvic grim sits the true (or lesser pelvis) whereas the false (or greater pelvis) is represented by the structure above it. As shown in Figure 2.2, posteriorly formed by the prominent anterior lip of the upper surface of the body of the sacrum, the pelvic grim also accounts, anteriorly, for the pubic crest and the upper edge of the pubic symphysis. The obturator foramen assures the anterolateral communication between the true pelvis and adductor region of the thigh being the first of three anatomical features with that purpose. It is a large opening in the anterior part of the hip bone with a complete bony boundary. The sacrotuberous and sacrospinous ligaments constitute the bridging between the greater and lesser sciatic notches, representing the remaining communication spots that form the true pelvis [10].

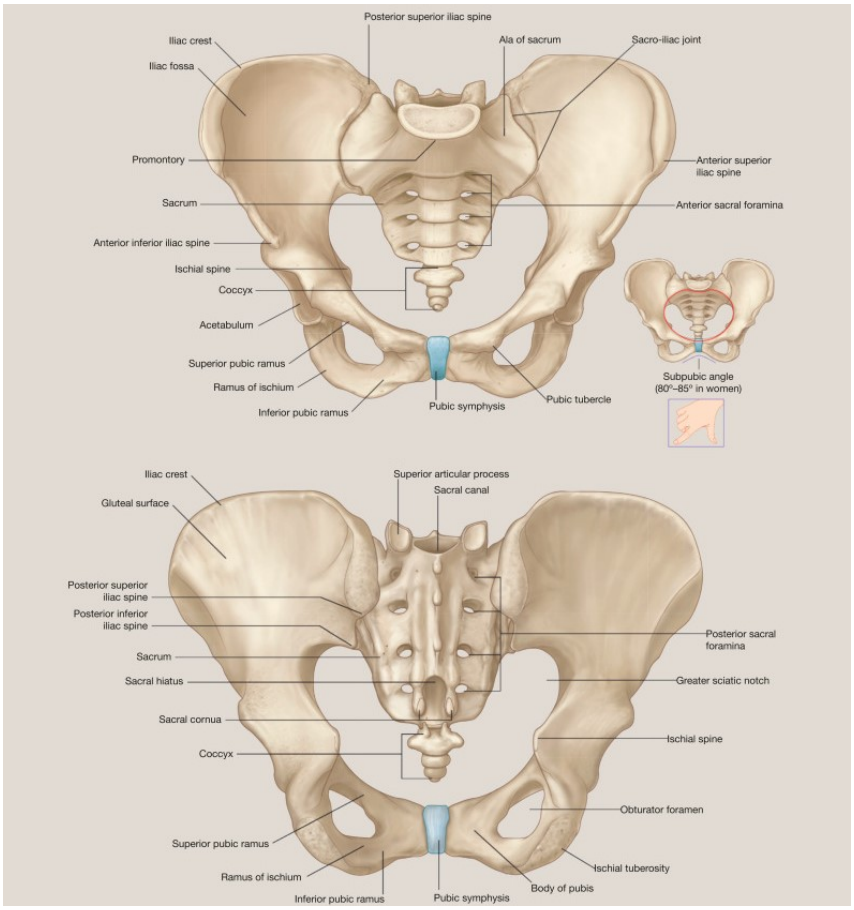


Figure 2.2: Anatomic features of the bony pelvis [10].

Lastly, three main functions enhance the importance of the bone cavity - Figure 2.5 [10]:

- Force transmission - transmitting the weight of trunk, upper limbs and head to the lower limbs, and the upward thrust generated by the lower limbs during locomotion to the vertebral column;

- Protection - the bony pelvis protects the pelvic viscera and vessels contained within it;

- Muscle attachment - providing anchorage through its external surface to several extremely powerful muscles such as the glutei, the adductors and the hamstrings.

### 2.1.2 Joints and Ligaments

There are four attached joints to the bony pelvis – the right and left sacroiliac joints, the pubic symphysis and the sacrococcygeal joint - Figure 2.3. Supported and stabilized by the sacrotuberous, sacrospinous, iliolumbar, and sacroiliac, these joints and ligaments may be described as follows [9] [10].

The sacroiliac joint is a plane synovial joint lying between the auricular surfaces of the ilium and the sacrum. The joint capsule is attached to the articular margins of both bones. In addition, numerous thick fibrous bands pass between the sacral and iliac auricular surfaces obliterating the joint cavity in places. Further reinforcement is assured by the anterior, interosseous, and posterior sacroiliac ligaments.

The pubic symphysis is a secondary cartilaginous joint standing in the middle of the right and left pubic bones. Articular surfaces of the two pubic bones are covered by a thin plate of hyaline cartilage, joined by thick and dense bands of fibrocartilage, form the fibrocartilaginous interpubic disc. This joint is reinforced by the superior pubic ligament superiorly and the arcuate pubic ligament inferiorly.

The sacrococcygeal joint works as a secondary cartilaginous one between the narrow inferior extremity of the sacrum and the superior surface of the coccyx. The joint is anteriorly supported by the anterior sacrococcygeal ligament and posteriorly by the posterior sacrococcygeal ligaments. On both sides lies a lateral sacrococcygeal ligament between the inferolateral angle of the sacrum and the transverse process of the coccyx.

The sacrotuberous ligament extends from the medial border of the ischial tuberosity to the posterior superior iliac spine, the posterior sacroiliac ligaments, and the lateral aspect of the sacrum and coccyx. The sacrotuberous ligament stabilizes the sacroiliac joint by preventing the tendency of the sacrum to be pushed anteroinferiorly by the vertebral column on account of the weight of the body above.

The sacrospinous ligament is a triangular ligament that lies deep to the sacrotuberous ligament. Its narrow apex is attached to the tip of the ischial spine and its broad base is attached to the side of the sacrococcygeal junction. The sacrospinous ligament and ischial spine together form a boundary between the greater and lesser sciatic foramina. The sacrotuberous and sacrospinous ligaments surround the lesser sciatic foramen.

The iliolumbar ligament extends from the fifth lumbar (L5) vertebra splitting laterally into two bands. The superior band that passes to the posterior

end of the iliac crest and the inferior band blend with the anterior sacroiliac ligament.

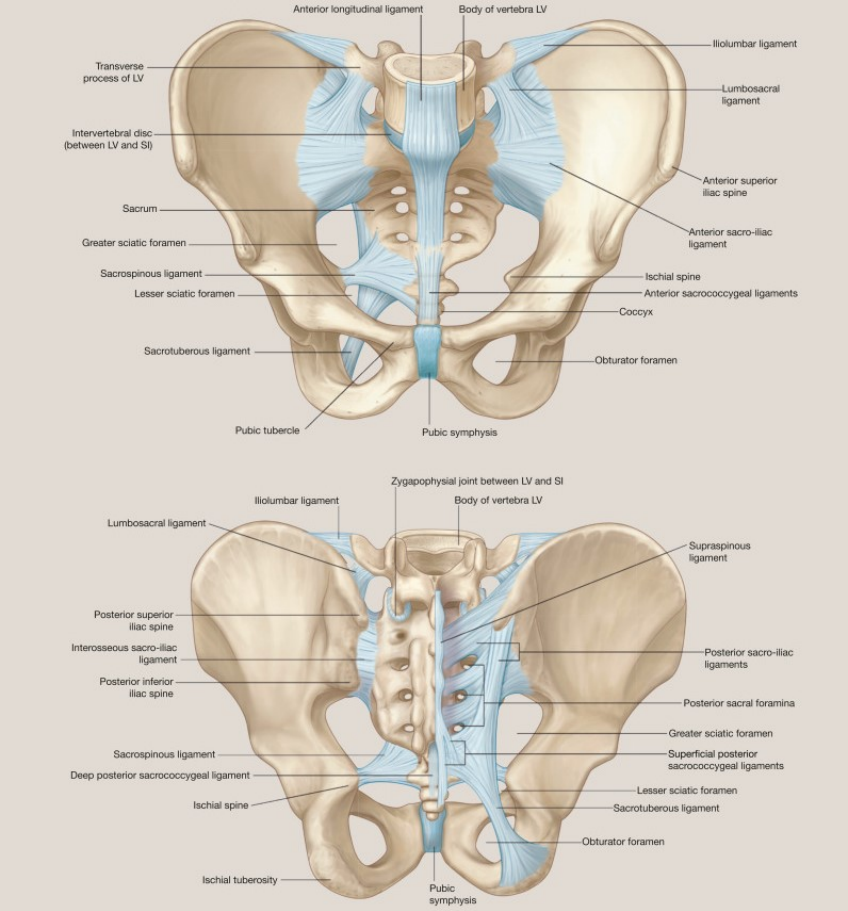


Figure 2.3: Joints and ligaments of the pelvis [10].

### 2.1.3 Muscles

The pelvic muscles, the ones attached to the bone cavity, can be split in two distinct groups: those that are attached to the bony pelvis outside the pelvic cavity - from the lower limb (adductors, hamstrings, the glutei, rectus femoris and others), from the anterior abdominal wall (external oblique, internal oblique and transversus abdominis), the iliacus and the numerous perineal muscles that are attached to the lower margin of the pelvic ring below the pelvic floor – as well as those situated inside the pelvic cavity, which deserve a greater focus on the current work's scope [10].

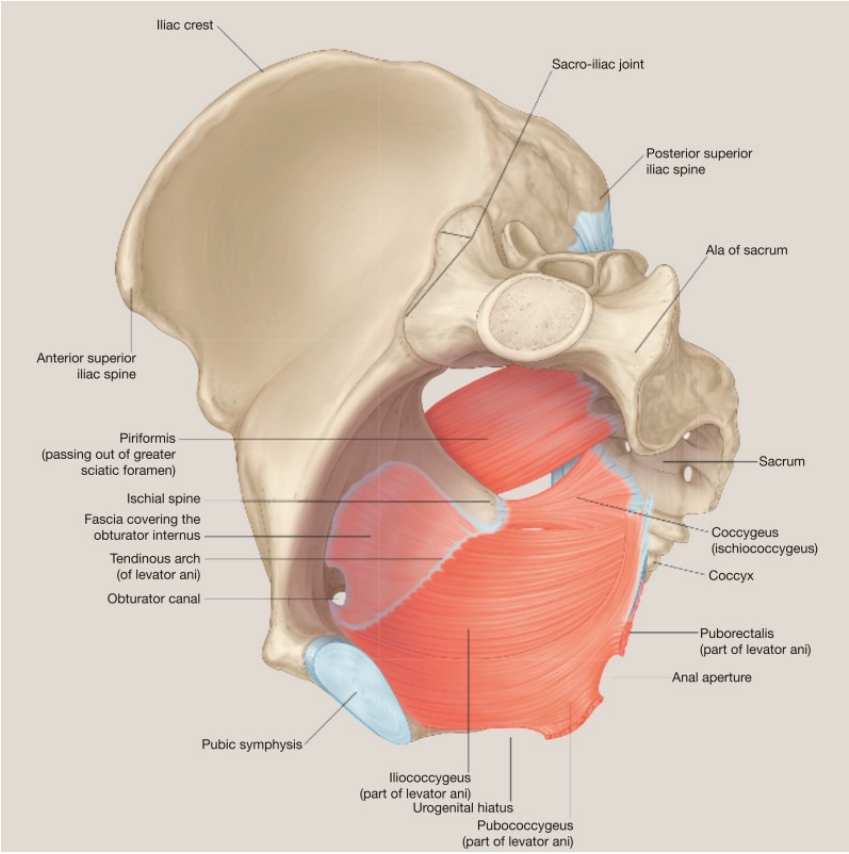


Figure 2.4: Muscles of the pelvic cavity [10].

The piriformis, the obturator internus, the coccygeus and the *levator ani* form the walls and floor of the pelvic cavity – the pronest region for the development of impairments. The pelvic wall is partly composed by the piriformis, rising from the front of the sacrum, and by the obturator internus, that arises from anterolateral aspect of the pelvic cavity on the inner surface of the obturator membrane and the bony margins of the obturator foramen. It is also important to notice the fact that these two muscles the tendons of these two muscles leave the interior of the bony pelvis to enter the gluteal region where both run immediately behind the capsule of the hip joint capsule before attaching to the greater trochanter of the femur. These two muscles work together as external rotators of the hip joint [11].

Regarding the pelvic floor, formed by the midline convergence of the coccygeus and the *levator ani* muscles, it may be seen as a muscular hammock on the bottom of the cavity. Whereas the coccygeus is a delicate muscle, extending from the tip of the ischial spine to the side of the sacrococcygeal junction, the *levator ani* is a larger and wider tissue. Arising from a linear thickening in the obturator fascia , the first runs inwards to interdigitate with the contralateral *levator ani* to form a mobile, thin, gutter-shaped muscular sheet, slung like a hammock from one side to the other. Finally, in an anterior position between the medial edges of the two *levator ani* muscles, the *levator*

*hiatus* (a natural gap) creates a passage for the rectum, urethra and the vagina [10].

### 2.1.4 Organs

The viscera present in the female pelvic cavity includes the distal third of sigmoid colon, the entire rectum, the urinary bladder, the intrapelvic segments of the right and left ureters, the uterus, the right and left uterine tubes, the right and left ovaries, and the intrapelvic portion of the vagina [11]. A common feature in both sexes is the urinary bladder being the most anterior viscus in the pelvic cavity and the terminal portion of the sigmoid colon and rectum the most posteriorly located of the intrapelvic viscera. The urinary bladder, along with the proximal urethra, is, consequently, particularly vulnerable in fractures and disruptions of the anterior circumference of the pelvic ring [10].

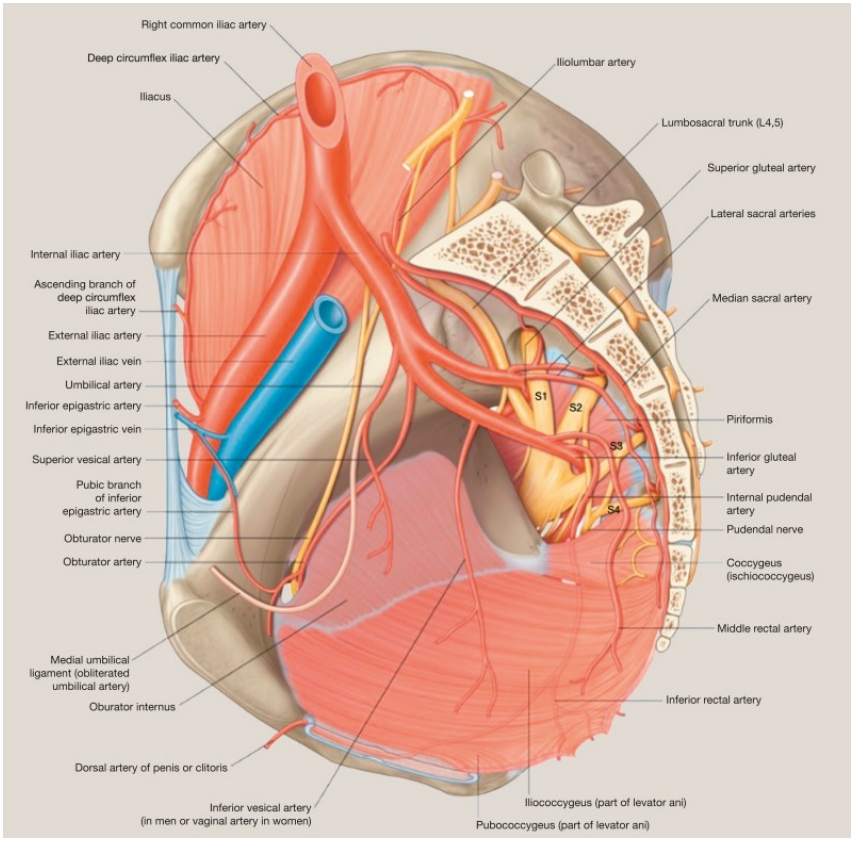


Figure 2.5: Female pelvic viscera and perineum [10].

## 2.2 Pelvic Organ Prolapse

### 2.2.1 Introduction

POP is a common pelvic floor dysfunction (PFD) associated with the degeneration of pelvic tissues usually related to hormonal changes, vaginal delivery, lifestyle and co-morbid factors or aging effects. POP is the descent of one or more of the anterior vaginal wall, posterior vaginal wall, the uterus (cervix), or the apex of the vagina (vaginal vault or cuff scar after hysterectomy). Prolapse of pelvic structures can cause a sensation of pelvic pressure or bulging through the vaginal opening and may be associated with urinary incontinence, voiding dysfunction, fecal incontinence, incomplete defecation, and sexual dysfunction [12]. It is estimated that POP prevalence ranges between 35 and 50% of women [4]. In fact, according to a survey [13], women have an 11% chance of requiring a surgery due to PFD's during their lifetime - either with synthetic or absorbable implants. Currently, this health condition leads to 300000 operations each year in the United States, with an anatomical recurrence rate of the prolapse of 31.3% ($grade > or = II$) [14]. Even though POP has been on medical record for millennia, dating back to 1835 B.C., an efficient treatment is yet to be achieved. The setbacks on this regard correlate to the complexity of the region and the nonexistence of a proper mimicking procedure of the mechanical properties shown by the natural tissues [6].

### 2.2.2 Types of Prolapse

Different types of Pelvic Prolapse are classified with regard to the pelvic organ presenting displacement due to tissue and ligament impairments inside the cavity. Considering the previously mentioned organs, Figure 2.6 represents the different types of prolapse.

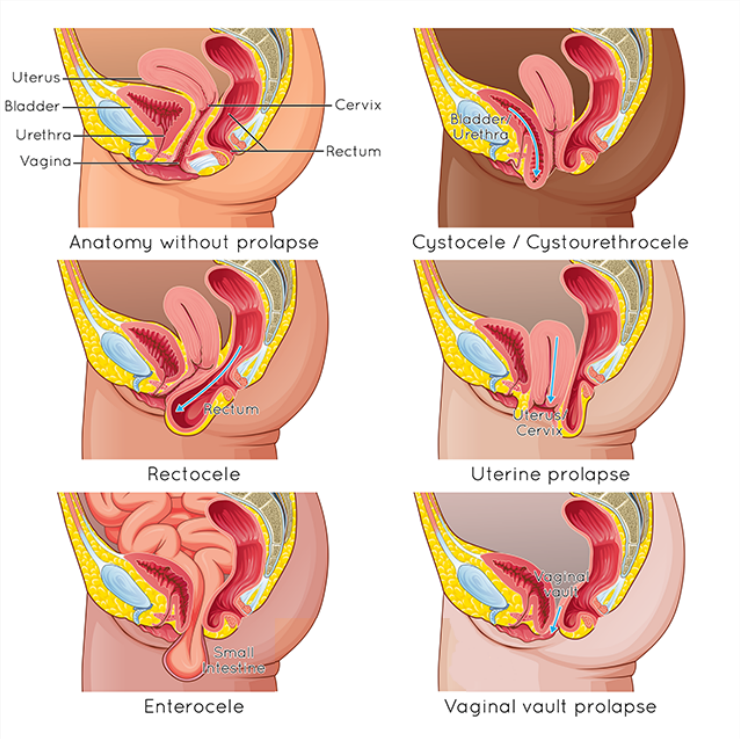


Figure 2.6: Types of pelvic organ prolapse [15].

The vaginal vault prolapsed is related to herniation of the vaginal vault (the expanded region of the vaginal canal at the internal end of the vagina) caused by the loss of support or weakening of specific ligaments, among other similar factors. The uterine prolapse, caused by the loss of support of some ligaments, is the herniation of the uterus. The cystocele consists in the herniation of the anterior vaginal wall and bladder. The enterocele corresponds to the herniation of the superior portion of the posterior vaginal wall caused by tearing and/or stretching of the posterior vaginal wall endopelvic fascia. The rectocele regards the herniation of the inferior portion of the posterior vaginal wall and rectum, having the same associated causes as the enterocele configuration [2].

### 2.2.3 Severity and Quantification

Thanks to an examination called POP-Q (Pelvic Organ Quantification), which measures the relative position of six points of the vagina to the hymen, it is possible to quantify and classify distinct stages of the advancement of a pelvic floor dysfunction. An example of a stage 0 prolapse, or absence of prolapse, is the situation of a patient whose cervix is located as low as the maximum of the vagina's length. From here, the classification is made depending on the the distance of the prolapsed organ to the hymen [16]. Figure 2.7, in turn, represents the six reference points of the vagina, used for the POP-Q.

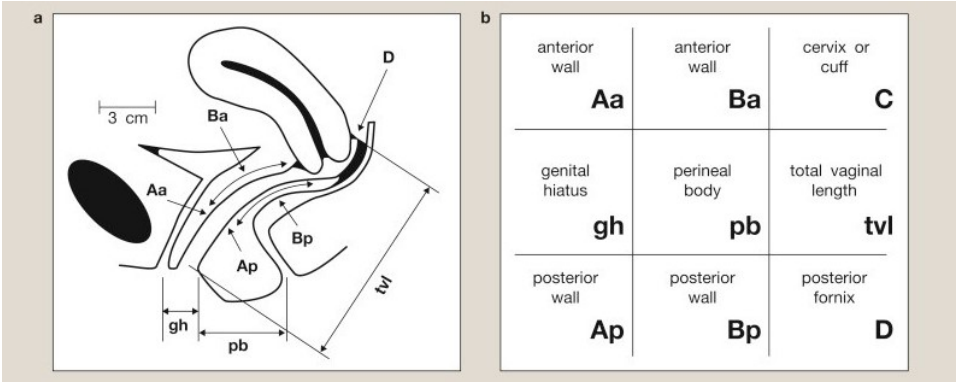


Figure 2.7: POP-Q system: a) Diagram of vaginal relative proportions and segments; b) Vaginal relative proportions and segments description [17].

The several stages in terms of distal portion measurement may be described as follows [2].

- Stage 0 - No prolapse;
- Stage I - The most distal portion of the prolapse is $\geq$1 cm above the level of the hymen;
- Stage II - The most distal portion of the prolapse is $\leq$1 cm proximal of distal to the hymen;
- Stage III - The most distal portion of the prolapse is $\geq$1 cm below the hymen but protrudes no further than 2 cm less than the total vaginal length;
- Stage IV - Complete eversion of the total length of the vagina, the distal portion protrudes at least the total vaginal length minus 2 cm beyond the hymen.

### 2.2.4 Epidemiology

Even though POP is one of the most common dysfunctions leading to gynaecological surgery, epidemiological studies of the incidence of this disorder are rare. Most of the available documentation relates either to clinical populations or and surgical registries or to other similar databases, built for surgically treated prolapsed identification. The number of women who have pelvic organ prolapse is expected to increase by 46%, to 4.9 million, by 2050 [12].

According to the literature [2], no epidemiological studies have been done of pelvic organ prolapse in community-based populations. Loss of vaginal or uterine support in women presenting for routine gynaecological care is seen in up to 43 to 76% of patients, with 3–6% having descent beyond the hymen [18]. In the Women's Health Initiative, 41% of women age 50 to 79 years

showed some amount of POP, including cystocoele in 34%, rectocoele in 19%, and uterine prolapse in 14% [19]. In a multi-centre study of 1006 women age 18–83 years presenting for routine gynaecological care, 24% had normal support and 38% had stage I, 35% stage II, and 2% stage III POP. It is, then, safe to conclude that some loss of uterovaginal support is present in most adult women.

There is no clear consensus, however, about what level of prolapse represents a variation of normal uterovaginal support and what represents disorder, although most people would agree that prolapse beyond the hymen is clinically significant [2]. A woman's lifetime risk of surgery for pelvic organ prolapse by age 80 years is about 7%, being the peak incidence of such surgery in individuals aged 60 to 69 years [20]. Still, almost 58% of procedures are undertaken in people younger than 60 years. According to a study conducted in the United Kingdom in 2011 [21], an estimated 19% of patients who had surgery would need a repeat operation within 5 years [14].

### 2.2.5 Etiology and Risk Factors

Research suggests many risk factors for POP [6]. Consequently, the cause of this disorder is recognized as a spectrum of several factors, varying from patient to patient. Advancing age and increasing weight are among the most consistent risk factors, but it is vaginal childbirth the one most frequently associated with prolapse. Increasing vaginal parity was denoted as the strongest risk factor for POP in women younger than 60 years [2]. Compared with individuals who had never given birth, a woman who had delivered two children sees twice as much risk of developing prolapsed. According to the Women's Health Initiative, a single childbirth is also associated with raised odds of uterine prolapse, cystocoele, and rectocele [22]. Every additional delivery up to five births increased the risk of worsening prolapse by 10–20[%]. Following these data, studies developed by the Pelvic Organ Support study and the Progetto Menopausa Italia, showed that the risk of POP increased with parity [23]. Table 2.1 shows the potential and established risk factors for the development of the condition. It is also important to understand the benefits of caesarean section parturition on reducing the risk of prolapse whereas forceps delivery enhances it [2], as well as the fact that the risk rises 3% per additional 100g of the newborn [24].

Table 2.1: Potential and established risk factors of POP

| | **Risk Factors** | **Established Risk Factors** |
|---|---|---|
| [2] | Vaginal delivery | Pregnancy, especially when followed by forceps delivery |
| | Advancing age | Young age at first delivery |
| | Obesity | Prolonged second stage of labour |

### 2.2.6 Treatment

Given the intricacies POP may cause on a woman's life quality, the importance of an efficient treatment is unquestionable. Even though each solution should theoretically answer to the specific problems of each patient, personalized medicine is yet to be fully in play for this kind of heath condition. Eventually, a detailed picture of the impairments' severity will allow more adequate solutions. For now, two types of treatment are considered, the conservative treatment, that is a less invasive option, and the surgical treatment. The last relies on a medical intervention on the impaired tissues, for which the associated procedures change depending on the type and stage of the prolapse [8].

#### 2.2.6.1 Conservative Treatment

The conservative approach is supported by the pessary, a prosthetic device that is inserted into the vagina for structural and pharmaceutical purposes. The pessary, built with silicone, is a safe and quiet efficient medical device, assuring a substantial improvement on the condition. This option is chosen as a temporary solution or when the presented symptoms do not force the woman to face the invasive option, surgery. The length of the instrument varies between 65 and 100 millimetres and it may be used either as a support or as a mere extra volume [25]. The support service is usually assured by the placement of an internal ring that may be seen in Figure 2.8, along with the representation of such placement. The ring model assures higher comfort than the three-dimensional version, which is deployed in more severe cases of POP [26]. However, as a downside of this approach, vaginal erosion and discharge, constipation and urinary incontinence are usual consequences of pessary implementation, which diminishes its prevalence [15].

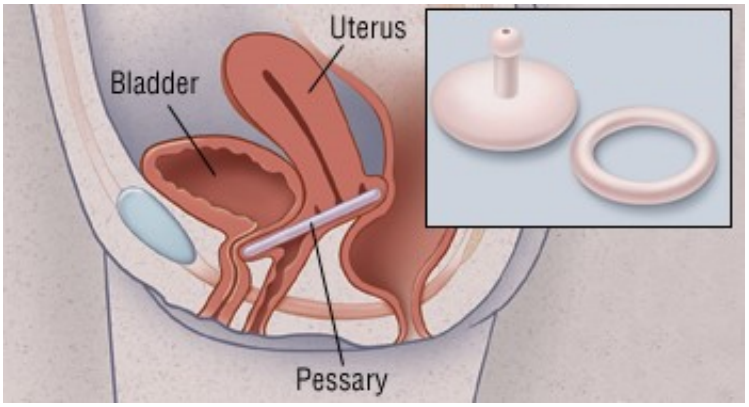


Figure 2.8: Pessary examples and a placement technique [26].

A different conservative approach is the rehabilitation therapy, used as a prevention technique so that POP incidence may be avoided beforehand. Basically relying on a healthy lifestyle, the woman is advised to improve her

physical shape, to avoid extreme efforts and engage in pelvic physiotherapy [25].

#### 2.2.6.2 Surgical Treatment

Surgery stands as the convenient option for patients with more severe symptoms, which cannot be solved through the conservative treatment options. In this case, a full reconstruction of the anatomy is intended, re-establishing functions and structures. Several techniques are used during the surgical procedure, and depend on the type, stage and general condition of the prolapsed. Nevertheless, two main differentiations are made with reconstructive type surgery - which aims at anatomic optimization - and obliterative type surgery - which permanently closes the vaginal canal [27]. Deciding on the most adequate technique for a specific case will depend on the state of the impairments, as previously said. In some cases the tissues will be accessed from the vagina - apical suspension and vaginal hysterectomy – whereas the sacrocolpopexy and sacred hysteropexy are related to abdominal interventions [28].

The anterior colporrhaphy is the most successful procedure for treating the anterior prolapse, reaching total repair in 80 to 100% of cases [29]. This technique is the median placation of the endopelvic fascia of the anterior vaginal wall. Regarding the suspension of the vaginal wall on the tendinous arch fascia, the surgical approach is the correction of the paravaginal defect [28]. The traditional posterior colporrhaphy, the site-specific posterior correction and the transanal correction are the methods for the treatment of posterior prolapse.

Finally, in terms of apical prolapse, the usual approaches are either the apical transvaginal suspension techniques – the suspension to the sacrospinous ligament and to the uterosacral ligaments - or the sacrocolpopexy, which fixates the vagina to the anterior longitudinal sacral ligament [28].

#### 2.2.6.3 Surgical Implants

Surgical meshes, the pelvic implants on which some of the procedures described rely, assure an extra support to the structures in order to compensate the impairments caused by prolapsed pelvic organs. The choice of mesh type lies between non-absorbable meshes (synthetic structures that are not biodegradable) and absorbable ones, which slowly dissolve within the body, allowing natural tissue to grow and consolidate the reinforcement of the ligaments and gradually replacing the mesh [30].

Native tissues used to be the most common solution but, given the relatively high failure rate with prolapsed relapses, surgeons turned to synthetic meshes [3]. The main reason for this being the fact that the implants were found to be damaging the involving biological tissues due to inappropriate levels of rigidity. Using polypropylene, which was quite successful in the correction of hernias, controversy eventually rose due to matters of safety and

effectiveness related to the treatment. Among these were vaginal bleeding, urinary infections and incontinence, pain and sensorial discomfort [30]. As a consequence, rates of recurrence for surgery started to climb, stressing the importance of properly address the properties and bioactivity of the implants. In 2019 the FDA actually prohibited the use of polypropylene for transvaginal repair of anterior POP [31].

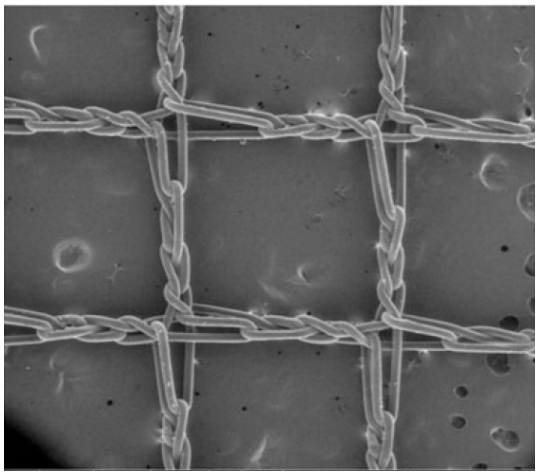

Figure 2.9: SEM image of the Restorelle® mesh [5].

Currently, innovative manufacturing techniques materialize the hope for reaching more efficient and less invasive mesh configurations. A commercially available option is the Restorelle® mesh - Figure 2.9 - composed by knitted monofilament with a pore dimension of 2 mm, showing a degradation time of 2 to 3 years inside the body [5]. Even though it does not perfectly match the mechanical behaviour of native tissues, it has received the FDA approval, which represents a major accomplishment [32].

## 2.3 Melt Electrospinning

The electrostatic drawing (electrospinning) of polymer fibers is a unique technology for the fabrication of one-dimensional (1D), two-dimensional (2D) and three-dimensional (3D) materials. Electrospinning manifested a rising scientific output with an almost exponential rise in publications over the last twenty years. The maturation of the field is acknowledged with corporate interest in diverse industry sectors such as air/water filtration and industrial areas relying on nano and sub-micron fibers with specific properties [33]. Moreover, the fields of tissue engineering and regenerative medicine, which constitute the framing for the current work, paved the way for the process's variant based on polymer melts (melt electrospinning) to approach proper economies of scale, having found ground on developing applications such as the replication of biologic structures and micro-structures [33]. In fact, the latest developments prove the feasibility of using this technique for the production of fibers that

allow cellular proliferation and growth, an essential feature for tissue engineering [34]. A general schematic representation of a printing set of this kind may be found in Figure 2.10.

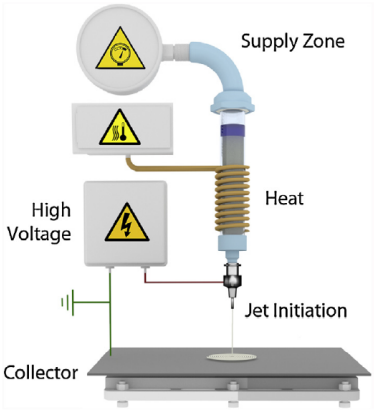


Figure 2.10: Melt electrospinning onto a static collector. A supply zone forces a molten polymer through a spinneret to a jet initiation point. A high voltage potential difference between the spinneret and collector induces an electrical force on the polymer emerging from the spinneret at the jet initiation point. The emerging polymer is then electrostatically drawn as a molten polymer jet to the collector where it solidifies as an ultrafine filament. The reader should notice here are many different melt electrospinning system design iterations (adapted from [33]).

It is known that this technology permits a precise and predictable fiber deposition in the combination with moving collectors, allowing the layer-by-layer fabrication of small to large volume scaffolds with specific designs, shapes and thicknesses [34]. For the case of the current work, the performance of the available 3D printer had already been studied [5]. With control over the device's parameters such as the temperature and rate of extrusion, voltage and the linear printing head speed, several geometries where printed and properly tested afterwards.

### 2.3.1 Biodegradable Poly $\epsilon$-caprolactone

Poly $\epsilon$-caprolactone (PCL) is a member of the biodegradable polyesters. As an aliphatic semi-crystalline polymer, its melting temperature ranges between 59 and 64°C and the glass transition occurs at -60°C. Consequently, at physiological temperature, the behaviour of the semi crystalline PCL shows high toughness and superior mechanical properties, having its elasticity as a function of the molecular weight. These characteristics, along with non-toxicity and tissue compatibility, are the reason for PCL being widely used as scaffolds in regenerative therapy [35].

Different mesh geometries may be accomplished using PCL in electrospinning writing, as Figure 2.11 demonstrates.

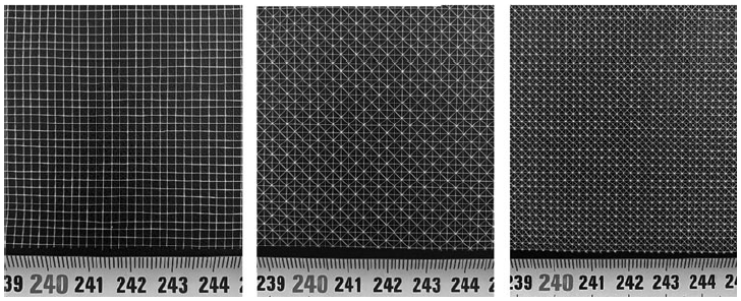


Figure 2.11: Melt electrospun printed meshes (square-shaped, triangular-shaped and cross shaped) [5].

# Chapter 3
# Computational Modelling

## 3.1 Introduction

This section not only embodies the first explanations of the active presence of computational assistance in the current work. It regards a theoretical contextualization for the Finite Element Method (FEM), widely used to perform stress analysis of structures and systems for which, due to the level of complexity, analytical solutions are difficult to obtain. These analyses have been used in many applications across several industry sectors including aerospace, automotive, architecture and, in recent years, biomedical engineering. Finite Element Analysis software is used to reduce the number of physical prototypes and experiments, allowing the development of more competitive products at a lower cost.

Before developing an efficient model, the whole mathematical context must be understood in order to simulate the involved material behaviours. The current work is also a characterization of PCL, where a continuum approach was used to describe the analysed bodies. Ultimately, the finite element method will accurately frame the mechanical stresses and strains present on the continuum bodies, defining them as a finite number of elements with simple geometries. This process aims at defining the material behaviour.

## 3.2 Preliminary Concepts

### 3.2.1 Continuum Bodies

Macroscopic systems are usually described with a continuum approach, which leads to the continuum theory. A fundamental statement derives from it assuming that a body, denoted by $B$, may be described as a continuous distribution of matter in space and time and it is considered to have a continuous composition of a set of particles, represented by $P \in B$. Consequently, mass and volume are continuous functions of continuum particles in a macroscopic study of a body, which is then known as a continuum body [36].

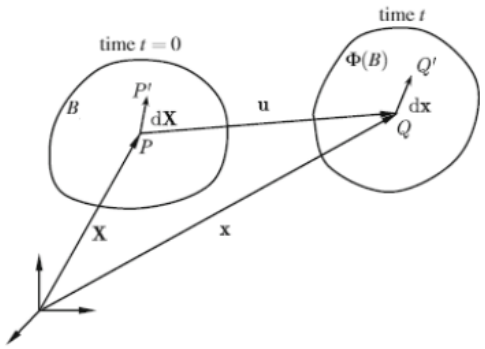


Figure 3.1: General motion of a deformable body [37].

Figure 3.1, a continuum body $B$ is represented with particle $P \in B$ inside the three-dimensional Euclidean space at a given instant of time $t$. The continuum body $B$ moves in space from one instant of time to another, and its placement is denoted as configuration $\mathbf{\Phi}(B)$ of body $B$ [36].

The configuration of the body $B$ maps the places of all the particles of $B$ in the Euclidean space. The motion of the body $B$ is related with the vector field $\mathbf{\Phi}$ that defines the new location $\mathbf{x}$ of a particle $\mathbf{X}$ for a fixed $t$:

$$\mathbf{x} = \mathbf{\Phi}(\mathbf{X}) \tag{3.1}$$

Considering a given particle $\mathbf{X}$ that occupies the position $(\mathbf{x};t)$, in a given instance, its position is a function of place $\mathbf{x}$ at time $t$:

$$\mathbf{X} = \mathbf{\Phi}^{-1}(\mathbf{x}) \tag{3.2}$$

### 3.2.2 Material and Spatial Descriptions

In finite deformation analysis, for the behavior of the body whose motion is under consideration to be described, a proper coordinate system must be selected. Given by Equation 3.1, the mentioned material (or referential) description is a characterization of the motion, or any other quantity, with respect to the material coordinates $X_1$; $X_2$; $X_3$ and time $t$. In the material description, also referred to as Lagragian description, the focus is a single particle in order to understand its movement.

Given by Equation 3.2, the so-called Eulerian (or spatial) description, refers to a characterization of the motion, or any other quantity, with respect to the spatial coordinates $x_1$; $x_2$; $x_3$ and time $t$. In this case, a point in space is the object of focus, as well as how time affects that exact point [36].

### 3.2.3 Deformation Gradient

Shape, position and orientation of a body generally change in the presence of motion. A continuum body is said to be deformable if it is able to change its shape [37]. In Equation 3.1 it is seen that, for a given point $P$ in the undeformed configuration, a unique point $P$ exists in the deformed configuration and a mapping relation, where $\mathbf{u}(\mathbf{X};t)$ is the displacement of point $P$, can be written as:

$$\mathbf{x} = \mathbf{\Phi}(\mathbf{X}, t) = \mathbf{X} + \mathbf{u}(\mathbf{X}, t) \tag{3.3}$$

Figure 3.1 shows neighboring points $P'$ and $Q'$ at infinitesimal distances from $P$ and $P$ that are denoted by vectors $d\mathbf{X}$ and $d\mathbf{x}$, respectively, in the two geometries. It is important to notice that the vector $d\mathbf{X}$ deforms to $d\mathbf{x}$. Assuming continuous mapping, the relationship between differential elements $d\mathbf{X}$ and $d\mathbf{x}$ can be expressed as follows:

$$d\mathbf{x} = \frac{\partial \mathbf{x}}{\partial \mathbf{X}} d\mathbf{X} \Rightarrow d\mathbf{x} = \mathbf{F} d\mathbf{X} \tag{3.4}$$

where $\mathbf{F}$ is the deformation gradient that maps elemental vectors of the reference configuration to elemental vectors in the spatial configuration. Known as a tensor, it associates a material line element $d\mathbf{X}$ in $B$ to the spatial line element $d\mathbf{x}$ in $\mathbf{\Phi}(B)$. If $\mathbf{F} = 1$, then $d\mathbf{X} = d\mathbf{x}$ and there is no deformation. An infinitesimal volume in the undeformed geometry can increase or decrease its size, but never shrink to a point, i.e., zero volume. Mathematically, this means that the determinant of deformation gradient, an important property to make a valid mapping of $\mathbf{\Phi}(\mathbf{X}, t)$ during large deformations must be positive [37]:

$$\det \mathbf{F} \equiv J > 0 \tag{3.5}$$

### 3.2.4 Strain Measures

It is now necessary to determine the material elements changes in terms of (second order) strain tensors associated with both reference and current configuration [38]. Considering the change in the scalar product of two elemental vectors $d\mathbf{X}_1$ and $d\mathbf{X}_2$, since they deform to $d\mathbf{x}_1$ and $d\mathbf{x}_2$, the changes in length and in the enclosed angle between the two vectors will be involved. Therefore, considering the Equation 3.4, the spatial scalar product $d\mathbf{x}_1 \cdot d\mathbf{x}_2$ may be written in terms of the material vectors $d\mathbf{X}_1$ and $d\mathbf{X}_2$:

$$d\mathbf{x}_1 \cdot d\mathbf{x}_2 = d\mathbf{X}_1 \cdot \mathbf{C} d\mathbf{X}_2 \tag{3.6}$$

where $\mathbf{C}$ corresponds to the right Cauchy-Green deformation tensor, also known as material tensor quantity, and it is given in terms of the deformation gradient $\mathbf{F}$ as:

$$\mathbf{C} = \mathbf{F}^T\mathbf{F} \tag{3.7}$$

Conversely, the initial material scalar product $d\mathbf{X}_1 \cdot d\mathbf{X}_2$ can be written in terms of the spatial vectors $d\mathbf{x}_1$ and $d\mathbf{x}_2$:

$$d\mathbf{X}_1 \cdot d\mathbf{X}_2 = d\mathbf{x}_1 \cdot \mathbf{b}^{-1} d\mathbf{x}_2 \tag{3.8}$$

where $\mathbf{b}$ is the left Cauchy-Green tensor and it is a spatial tensor quantity:

$$\mathbf{b} = \mathbf{F}\mathbf{F}^T \tag{3.9}$$

The change in scalar product can be found in terms of the material vectors $d\mathbf{X}_1$ and $d\mathbf{X}_2$ and the Lagrangian strain tensor $\mathbf{E}$ as:

$$\frac{1}{2}\left(d\mathbf{x}_1 \cdot d\mathbf{x}_2 - d\mathbf{X}_1 \cdot d\mathbf{X}_2\right) = d\mathbf{X}_1 \cdot \mathbf{E} d\mathbf{X}_2 \tag{3.10}$$

where the material tensor $\mathbf{E}$ is

$$\mathbf{E} = \frac{1}{2}(\mathbf{C} - \mathbf{I}) \tag{3.11}$$

Alternatively, the same change in scalar product can be expressed with reference to the spatial elemental vectors $d\mathbf{x}_1$ and $d\mathbf{x}_2$ and the Eulerian strain tensor $\mathbf{e}$ as:

$$\frac{1}{2}\left(d\mathbf{x}_1 \cdot d\mathbf{x}_2 - d\mathbf{X}_1 \cdot d\mathbf{X}_2\right) = d\mathbf{x}_1 \cdot \mathrm{e} d\mathbf{x}_2 \tag{3.12}$$

where the material tensor $\mathbf{e}$ corresponds to

$$\mathbf{e} = \frac{1}{2}(\mathbf{I} - \mathbf{b}^{-1}) \tag{3.13}$$

### 3.2.5 Stress Measures

Stress is the physical dimension of force per unit area and responsible for material deformation. Motion and deformation originate interactions between the material and neighboring material in the inferior part of the body. Clarifying the used area, when a large deformation occurs, is crucial once the definition of stress depends on it [38].

A deformable body is considered during a finite motion and, for that body, a traction vector $\mathbf{t}$ can be defined using the area of the differential element $da$, the force $d\mathbf{f}$ acting on it, and the unit normal vector $\mathbf{n}$ of the area as:

$$\mathbf{t} = \lim_{da \to 0} \frac{d\mathbf{f}}{da} = \boldsymbol{\sigma}\mathbf{n} \tag{3.14}$$

where $\sigma$ is the Cauchy stress tensor, which is always symmetric and refers to the deformed geometry as a reference for both force and area. There are six

independent stress components acting at a certain point of a body, with $\sigma_{12} = \sigma_{21}$; $\sigma_{13} = \sigma_{31}$; $\sigma_{23} = \sigma_{32}$. For each stress component $\sigma_{ij}$, the convention states that the first index characterizes the component of the vector $\mathbf{t}$ at a certain point in the direction of the associated base vector $\mathbf{e}_i$, and the second index characterizes the plane that $\mathbf{t}$ is acting on, which is described by the direction of the base vector $\mathbf{e}_j$, as can be seen in Figure 3.2.

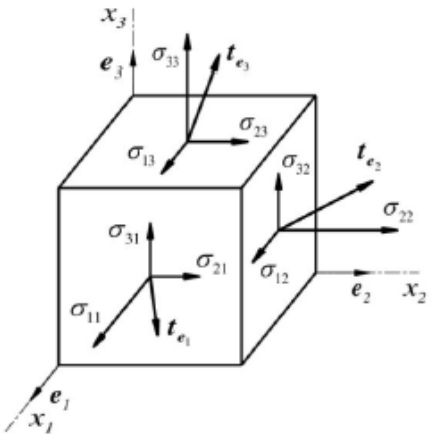


Figure 3.2: Positive stress components of the traction vectors $\mathbf{t}_{e_i}$ [36].

For the stress tensors based on the undeformed geometry to be defined, it is necessary to know both configurations. This enables the possibility of defining the Kirchhoff stress from the Cauchy stress as follows:

$$\boldsymbol{\tau} = J\boldsymbol{\sigma} \tag{3.15}$$

where $J$ represents its Jacobian defined by $J = det\mathrm{F}$.

Considering the same force $\mathbf{f}$, the differential area $dA$ and the unit normal $\mathbf{N}$ in the undeformed geometry, another traction vector $\mathbf{t}$ may be defined as:

$$\mathbf{T} = \lim_{dA \to 0} \frac{d\mathbf{f}}{dA} = \mathbf{P}^T\mathbf{N} \tag{3.16}$$

where $\mathbf{P}$ is known as the first Piola-Kirchhoff stress tensor; the force is associated with the deformed geometry and the area with the undeformed geometry.

Furthermore, the relationship between the Cauchy stress tensor and the first Piola-Kirchhoff stress tensor can be obtained as follows:

$$\mathbf{P} = J\boldsymbol{\sigma}\mathbf{F}^{-T} \tag{3.17}$$

The first Piola-Kirchhoff stress tensor will not be symmetric once the deformation gradient is not symmetric in the first place. This particularity,

which restricts its use, led to the definition of the material or Second Piola-Kirchhoff stress tensor:

$$\mathbf{S} = \mathbf{P}\mathbf{F}^{-T} = J\mathbf{F}^{-1}\boldsymbol{\sigma}\mathbf{F}^{-T} \tag{3.18}$$

The second Piola-Kirchhoff stress tensor is symmetric, measuring force per unit undeformed, exclusively assuming forces that act within the undeformed solid.

## 3.3 Principle of Virtual Power

Problems in computational mechanics usually aim at finding an approximate (finite element) solution for deformations, displacements, forces, stresses, etc, in a solid body subjected to specific events. To find the exact solutions, the force and moment equilibrium must be maintained over an arbitrary volume of the body [39].

The principle of conservation of linear momentum states that the rate of change of the total linear momentum of a continuum medium is equal to the vector sum of all external forces acting on the body. In the following equation of motion:

$$\frac{\partial \boldsymbol{\sigma}}{\partial \mathbf{x}} + \mathbf{f} = \rho \frac{\partial^2 \mathbf{u}}{\partial t^2} \tag{3.19}$$

where $\rho$ represents the mass density of the deformed solid, $\mathbf{f}$ the body force vector (per unit volume) and $\sigma$ the Cauchy stress distribution. These equations, Cauchy's Equations of Motion, must be satisfied for any continuum in motion. Without acceleration, the following static equilibrium equation is obtained:

$$\frac{\partial \boldsymbol{\sigma}}{\partial \mathbf{x}} + \mathbf{f} = 0 \tag{3.20}$$

The principle of virtual work [40] is another method for writing partial differential equations for linear moment balance in an equivalent integral form. Thus, it constitutes the basis for the finite element method, corresponding to the equilibrium of the work done by both internal and external forces with small, arbitrary and virtual displacements, which satisfy kinematic constraints.

For a deformable solid, subjected to a loading that induces a displacement field $\mathbf{u}(x)$ and a velocity field $\mathbf{v}(x)$, the loading consists of a prescribed displacement on a part of the boundary ($S_1$) and a traction $\mathbf{t}$ applied to the rest of the boundary ($S_2$). The loading induces a Cauchy stress and its distribution within the solid is denoted by $\sigma_{ij}$.

It is necessary to define a kinematically admissible velocity field $\delta\mathbf{v}(\mathbf{x})$, satisfying $\delta\mathbf{v} = 0$ on ($S_1$), which corresponds to an arbitrary differentiable vector field. The virtual velocity gradient and stretch rate are respectively represented as:

$$\delta\mathbf{L} = \frac{\partial \delta\mathbf{v}}{\partial \mathbf{x}} \tag{3.21}$$

$$\delta\mathrm{D} = \frac{1}{2}\left(\frac{\partial \delta\mathbf{v}}{\partial \mathbf{x}} + \left(\frac{\partial \delta\mathbf{v}}{\partial \mathbf{x}}\right)^T\right) \tag{3.22}$$

Objectively, the principle of virtual work can be stated as a case in which the stress, body force and traction are in equilibrium if, and only if, the rate of the work done by Cauchy stresses on the rate of deformation of any virtual velocity field are equal to the rate of work done by the traction and body forces acting on the body (external forces). Therefore, the principle of virtual work can be written as:

$$\int_V \boldsymbol{\sigma} : \delta\mathbf{D} dV + \int_V \rho \frac{\mathrm{d}\mathbf{v}}{\mathrm{d}t} \delta\mathbf{v} dV = \int_V \mathbf{f}\delta\mathbf{v} dV + \int_{S_2} \mathbf{t}\delta\mathbf{v} dA \tag{3.23}$$

The Gauss's theorem may be applied to prove this result since it defines a quality relationship between surface integrals and volume integrals:

$$\int_S \mathbf{n} \cdot ()dS = \int_V \frac{\partial}{\partial \mathbf{x}} \cdot ()dV \tag{3.24}$$

where ( ) is any continuous function-scalar, vector or tensor. Also, some statements regarding the properties of the Cauchy Stress can be used:

$$\sigma_{ij}\delta D_{ij} = \frac{1}{2}\sigma_{ij}\left(\frac{\partial \delta v_i}{\partial x_j} + \frac{\partial \delta v_j}{\partial x_i}\right) = \frac{1}{2}\left(\sigma_{ji}\frac{\partial \delta v_i}{\partial x_j} + \sigma_{ij}\frac{\partial \delta v_j}{\partial x_i}\right) = \sigma_{ji}\frac{\partial \delta v_i}{\partial x_j} = \frac{\partial}{\partial x_j}\left(\sigma_{ji}\delta v_i\right) - \frac{\partial \sigma_{ji}}{\partial x_j}\delta v_i \tag{3.25}$$

Applying these to the first term on the right-hand side of the principle of virtual work:

$$\int_V \boldsymbol{\sigma} : \delta\mathbf{D} dV = \int_V \frac{\partial \boldsymbol{\sigma}\delta\mathbf{v}}{\partial \mathbf{x}} dV - \int_V \frac{\partial \boldsymbol{\sigma}}{\partial \mathbf{x}}\delta\mathbf{v} dV \tag{3.26}$$

Applying the Gauss theorem to the same term and replacing it in Equation 3.23:

$$\int_{S_2} (\boldsymbol{\sigma}\cdot\mathbf{n})\delta\mathbf{v} dA - \int_V \frac{\partial \boldsymbol{\sigma}}{\partial \mathbf{x}}\delta\mathbf{v} dV + \int_V \rho\frac{\mathrm{d}\mathbf{v}}{\mathrm{d}t}\delta\mathbf{v} dV = \int_V \mathbf{f}\delta\mathbf{v} dV + \int_{S_2} \mathbf{t}\delta\mathbf{v} dA \tag{3.27}$$

Concerning the Equation 3.14, it is obtained:

$$\int_V \mathbf{f}\delta\mathbf{v} dV + \int_V \frac{\partial \boldsymbol{\sigma}}{\partial \mathbf{x}}\delta\mathbf{v} dV = \int_V \rho\frac{\mathrm{d}\mathbf{v}}{\mathrm{d}t}\delta\mathbf{v} dV \tag{3.28}$$

## 3.4 Constitutive Equations

Material straining is the concept behind the stresses produced in a body, as a result of the deformation of the material. Constitutive models aim to develop mathematical models for representing the real behavior of matter, depending on the type of material under consideration. They can be dependent or independent of time and, even though they may also satisfy certain physical principles, experimental measurements usually support these models since they cannot be calculated using fundamental physical laws.

### 3.4.1 Linear Elasticity

Generally, the constitutive behaviour of elastic materials is exclusively a function of the current state of deformation. This implies that any stress measure at a particle is a function of the current deformation gradient $\mathbf{F}$ associated with that particle. Alternatively, when the work done by the stresses during a deformation process is dependent only on the initial state at time t0 and the final configuration at time t, the behavior of a material is said to be path-independent and it is called hyperelastic [38].

### 3.4.2 Hyperelasticity

A hyperelastic material assumes the existence of a Helmholtz free-energy function $\Psi$, which is defined per unit undeformed volume. When $\Psi = \Psi(\mathbf{F})$ is a function of $\mathbf{F}$ or some strain tensor, the Helmholtz free-energy function is referred to as the strain-energy function or stored-energy function and the first Piola-Kirchhoff stress tensor can be calculated as [36]:

$$\mathbf{P} = \frac{\partial \boldsymbol{\Psi}(\mathbf{F})}{\partial \mathbf{F}} \tag{3.29}$$

Assuming the material can be defined through $\Psi$, which in turn is obtained from physical experiments, the symmetric Cauchy stress tensor, i.e,
$\sigma = J^{-1}\mathbf{P}\mathbf{F}^T = \sigma^T$

$$\sigma = J^{-1}\mathbf{F}\left(\frac{\partial \Psi(\mathbf{F})}{\partial \mathbf{F}}\right)^T \tag{3.30}$$

The strain-energy function can be represented in equivalent forms. Once $\Psi$ remains invariant under rigid body rotations, it is independent of the rotational part of $\mathbf{F} = \mathbf{R}\mathbf{U}$. Consequently, it can be concluded that a hyperelastic material depends on the stretching part of $\mathbf{F}$, i.e. the symmetric right stretch tensor $\mathbf{U}$.

Since the right Cauchy-Green tensor and the Green-Lagrange strain tensor are given by $\mathbf{C}{=}\mathbf{U}^2$ and $\mathbf{E} = (\mathbf{U}^2 - \mathbf{I})/2$, $\Psi$ may be expressed as a function of the six components of the symmetric material tensors $\mathbf{C}$, $\mathbf{E}$, respectively:

$$\mathbf{\Psi}(\mathbf{F}) = \mathbf{\Psi}(\mathbf{C}) = \mathbf{\Psi}(\mathbf{E}) \tag{3.31}$$

Reducing the constitutive equations for hyperelastic materials at finite strains, one may deduce:

$$\left(\frac{\partial \Psi(\mathbf{F})}{\partial \mathbf{F}}\right)^T = 2\frac{\partial \Psi(\mathbf{C})}{\partial \mathbf{C}}\mathbf{F}^T \tag{3.32}$$

which gives an important reduced form of the constitutive equation for hyperelastic materials, namely:

$$\sigma = J^{-1}\mathbf{F}\left(\frac{\partial \Psi(\mathbf{F})}{\partial \mathbf{F}}\right)^T = 2J^{-1}\mathbf{F}\frac{\partial \Psi(\mathbf{C})}{\partial \mathbf{C}}\mathbf{F}^T \tag{3.33}$$

Alternative expressions may be obtained for the Piola-Kirchhoff stress tensors $\mathbf{P}$ (not symmetric) and $\mathbf{S}$ (symmetric):

$$\mathbf{P} = 2\mathbf{F}\frac{\partial \mathbf{\Psi}(\mathbf{C})}{\partial \mathbf{C}} \tag{3.34}$$

$$\mathbf{S} = 2\frac{\partial \mathbf{\Psi}(\mathbf{C})}{\partial \mathbf{C}} = \frac{\partial \mathbf{\Psi}(\mathbf{E})}{\partial \mathbf{E}} \tag{3.35}$$

#### 3.4.2.1 Isotropic Hyperelastic Materials

Isotropy is a property of a specific type of materials which response, when studied in a stress-strain experiment, is the same in all directions. This means that the strain-energy function can be restricted by a particular property of the material. One example of an approximation to an isotropic material with a wide range of applications is rubber [36].

Taking into account the Lagragian description, the constitutive relation must be independent of the coordinate frame selected, since the material has the same property in all directions [36][38]. The associated necessary condition is $\Psi$ being only a function of the invariants of $\mathbf{C}$:

$$\mathbf{\Psi}(\mathbf{C}, \mathbf{X}) = \mathbf{\Psi}(I_1, I_2, I_3, X) \tag{3.36}$$

Which may be defined as,

$$I_1(\mathbf{C}) = t\mathbf{r}(\mathbf{C}) \tag{3.37}$$

$$I_2(\mathbf{C}) = \frac{1}{2}(\mathbf{I_1}^2 - \mathbf{C} : \mathbf{C}) \tag{3.38}$$

$$I_3(\mathbf{C}) = \det(\mathbf{C}) = J^2 \tag{3.39}$$

Making use of the chain rule of differentiation:

$$\frac{\partial \Psi(\mathbf{C})}{\partial \mathbf{C}} = \frac{\partial \Psi}{\partial I_1}\frac{\partial I_1}{\partial \mathbf{C}} + \frac{\partial \Psi}{\partial I_2}\frac{\partial I_2}{\partial \mathbf{C}} + \frac{\partial \Psi}{\partial I_3}\frac{\partial I_3}{\partial \mathbf{C}} \tag{3.40}$$

The derivates of the invariants with respect to $\mathbf{C}$ can be obtained after some algebraic calculations. Recalling the constitutive e Equation 3.35 and substituting these derivates into Equation 3.40, the second Piola-Kirchhoff stress may be presented as:

$$\mathbf{S} = 2\left[\left(\frac{\partial \Psi}{\partial I_1} + I_1\frac{\partial \Psi}{\partial I_2}\right)\mathbf{I} - \frac{\partial \Psi}{\partial I_2}\mathbf{C} + I_3\frac{\partial \Psi}{\partial I_3}\mathbf{C}^{-1}\right] \tag{3.41}$$

The previous equation may be used, for the case of isotropic hyperelastic materials, to obtain the spatial counterpart of the constitutive equation. Equation 3.18 gives the relationship between the Cauchy stress and the second Piola-Kirchhoff stress. Replacing $\mathbf{S}$ in this relation by Equation 3.41 and multiplying the tensor variables $\mathbf{I}$, $\mathbf{C}$, $\mathbf{C}^{-1}$ and $\mathbf{F}^T$ from the right hand side and $\mathbf{F}$ from the left hand side, the following equation, in terms of the left Cauchy-Green tensor $\mathbf{B}$, comes:

$$\boldsymbol{\sigma} = 2J^{-1}\left[\left(\frac{\partial \Psi}{\partial I_1} + I_1\frac{\partial \Psi}{\partial I_2}\right)\mathbf{b} - \frac{\partial \Psi}{\partial I_2}\mathbf{b}^2 + I_3\frac{\partial \Psi}{\partial I_3}\mathbf{I}\right] \tag{3.42}$$

Nevertheless this expression involves derivates with respect to the invariants of the material tensor $\mathbf{C}$. Since $\mathbf{b}$ and $\mathbf{C}$ have the same eigenvalues, their invariants are identical:

$$\mathbf{I_1}(\mathbf{b}) = tr(\mathbf{b}) = tr(\mathbf{C}) = \mathbf{I_1}(\mathbf{C}) \tag{3.43}$$

$$\mathbf{I_2}(\mathbf{b}) = \frac{1}{2}(\mathbf{I_1}^2 - \mathbf{b} : \mathbf{b}) = \frac{1}{2}(\mathbf{I_1}^2 - \mathbf{C} : \mathbf{C}) = \mathbf{I_2}(\mathbf{C}) \tag{3.44}$$

$$\mathbf{I_3}(\mathbf{b}) = \det(\mathbf{b}) = J^2 = \det(\mathbf{C}) = \mathbf{I_3}(\mathbf{C}) \tag{3.45}$$

Consequently, the derivates from Equation 3.42 also relate to the invariants of $\mathbf{b}$.

If the strain-energy function $\Psi$ is an invariant, $\Psi$ is also a function of the principal stretches and can be represented in the form:

$$\boldsymbol{\Psi} = \boldsymbol{\Psi}(\mathbf{C}) = \boldsymbol{\Psi}(\lambda_\mathbf{1}, \lambda_\mathbf{2}, \lambda_\mathbf{3}) \tag{3.46}$$

Considering,

$$\mathbf{I} = \sum_{a=1}^{3} \hat{\mathbf{N}}_a \otimes \hat{\mathbf{N}}_a \tag{3.47}$$

$$\mathbf{C}^{-1} = \sum_{a=1}^{3} \lambda_a^{-2}\hat{\mathbf{N}}_a \otimes \hat{\mathbf{N}}_a \tag{3.48}$$

And substituing these equations into Equation 3.41, the second Piola-Kirchhoff stress tensor is obtained:

$$\mathbf{S} = \sum_{a=1}^{3} \left( 2\frac{\partial \Psi}{\partial I_1} + 4\frac{\partial \Psi}{\partial I_2}\lambda_a^2 + 2I_3\frac{\partial \Psi}{\partial I_3}\lambda_a^{-2} \right) \hat{\mathbf{N}}_a \otimes \hat{\mathbf{N}}_a \tag{3.49}$$

Since $\lambda_a^2$ are the eigenvalues of $\mathbf{C}$, the invariants may also be obtained by:

$$I_1 = \lambda_1^2 + \lambda_2^2 + \lambda_3^2 \tag{3.50}$$

$$I_2 = \lambda_1^2\lambda_2^2 + \lambda_1^2\lambda_3^2 + \lambda_2^2\lambda_3^2 \tag{3.51}$$

$$I_3 = \lambda_1^2\lambda_2^2\lambda_3^2 \tag{3.52}$$

After differentiating these equations and substituting them into Equation 3.49, the following expression is reached using the chain rule:

$$\mathbf{S} = \sum_{a=1}^{3} S_{aa}\hat{\mathbf{N}}_a \otimes \hat{\mathbf{N}}_a; \quad S_{aa} = 2\frac{\partial \Psi}{\partial \lambda_a^2} \tag{3.53}$$

Taking into account the relationship with the second Piola-Kirchhoff stress tensor, the Cauchy stress is achieved once again:

$$\boldsymbol{\sigma} = J^{-1}\mathbf{F}\mathbf{S}\mathbf{F}^T = \sum_{a=1}^{3} \frac{2}{J}\frac{\partial \Psi}{\partial \lambda_a^2} \left(\mathbf{F}\hat{\mathbf{N}}_a\right) \otimes \left(\mathbf{F}\hat{\mathbf{N}}_a\right) \tag{3.54}$$

#### 3.4.2.2 Incompressible Hyperelastic Materials

Incompressible materials [36][38] can sustain finite strains without noticeable volume changes. Volume is kept constant throughout a motion as these materials are characterized by the incompressibility constraint:

$$\mathbf{J} = 1 \tag{3.55}$$

To obtain the general constitutive equations for incompressible hyperelastic materials, the strain energy function is given by:

$$\boldsymbol{\Psi} = \boldsymbol{\Psi}(\mathbf{F}) - p(\mathbf{J} - 1) \tag{3.56}$$

where the strain-energy $\Psi$ is defined for $\mathbf{J} = \det \mathbf{F} = 1$ and the scalar $p$ serves as an indeterminate Lagrange multiplier, known as a hydrostatic pressure, that may only be determined from the equilibrium equations and the boundary conditions.

Differentiating Equation 3.56 with respect to $\mathbf{F}$ and acknowledging the following equation:

$$\frac{\partial J}{\partial \mathbf{F}} = J\mathbf{F}^T \tag{3.57}$$

a constitutive equation for the first Piola-Kirchhoff stress tensor $\mathbf{P}$ can be obtained:

$$\mathbf{P} = -p\mathbf{F}^T + \frac{\partial \Psi(\mathbf{F})}{\partial \mathbf{F}} \tag{3.58}$$

Multiplying the previous equation by $\mathbf{F}^{-1}$ on the left hand side, the second Piola-Kirchhoff stress $\mathbf{S}$ is obtained:

$$\mathbf{S} = -p\mathbf{F}^{-1}\mathbf{F}^T + \mathbf{F}^{-1}\frac{\partial \Psi(\mathbf{F})}{\partial \mathbf{F}} = -p\mathbf{C}^{-1}\frac{\partial \Psi(\mathbf{C})}{\partial \mathbf{C}} \tag{3.59}$$

Conversely, for the case where Equation 3.58 is multiplied by $\mathbf{F}^T$ from the right hand side, the Cauchy stress comes as:

$$\boldsymbol{\sigma} = -p\mathbf{I} + \frac{\partial \Psi(\mathbf{F})}{\partial \mathbf{F}}\mathbf{F}^T = -p\mathbf{I} + \mathbf{F}e\frac{\partial (\mathbf{F})^T}{\partial \mathbf{F}} \tag{3.60}$$

## 3.5 Finite Element Method

The finite element method is one of the numerical methods used for solving differential equations that describe many engineering problems. For these problems to be solved with the finite element method, the domain of the body is divided into small segments known as elements. Each element has a set of nodes that are used to connect this element with other elements, sequentially used in the discretization of the body. The displacement of the material points of an element is approximated using a set of shape functions, the displacements of the nodes and, potentially, their derivates with respect to the spatial coordinates.

Relying on the principle of virtual work, the finite element formulation delivers the equilibrium equations. For a given material and loading conditions, the solution is given by a deformed configuration in a state of equilibrium. To obtain this new equilibrium position, the Netwon-Raphson iterative solution is applied, which requires the linearization of the virtual work [37] [39].

### 3.5.1 Discretized Equilibrium Equations

The displacement field can be approximated by interpolation functions (shape functions), where $n$ denotes the number of nodes per element, [39] and it is demonstrated as follows:

$$\mathbf{u}(\mathbf{X}) \approx \sum_{i=1}^{n} N_i(\mathbf{X})\mathbf{u}_i \tag{3.61}$$

In the expression above, at the beginning of each iteration, the position vector is represented by $\mathbf{X}$, the shape functions defined within the finite element correspond to $N_i(\mathbf{X})$ and $\mathbf{u}_i$ represents the unknown nodal displacement. Considering the interpolation of equation 3.61 and the fact that the virtual field $\delta\mathbf{u}$ must be compatible with all kinematics constraints, it can be written as:

$$\delta\mathbf{u}(\mathbf{X}) \approx \sum_{i=1}^{n} N_i(\mathbf{X})\delta\mathbf{u}_i \tag{3.62}$$

Rewriting the virtual work from equation 3.23 in terms of the virtual displacement:

$$\delta W = \int_V \sigma : \delta e dV - \int_V \mathbf{f} \cdot \delta\mathbf{u} dV - \int_{S_2} \mathbf{t} \cdot \delta\mathbf{u} dA \tag{3.63}$$

Equation 3.63 can be approximated by a variation over the finite set of $\delta\mathbf{u}_i$, from the discretization process. Thus, for an arbitrary node (a) of the element (e), it may be written by:

$$\delta W^{(e)} = \int_{V^{(e)}} \boldsymbol{\sigma} : (\delta\mathbf{u}_a \otimes N_a)\, dV - \int_{V^{(e)}} \mathbf{f} \cdot (N_a \delta\mathbf{u}_a)\, dV - \int_{S_2^{(e)}} \mathbf{t} \cdot (N_a \delta\mathbf{u}_a)\, dA \tag{3.64}$$

Equation 3.64 can be rearranged since the virtual nodal displacement is independent of the integration. Plus, the virtual work per element (e) per node (a) can be expressed in terms of internal and external equivalent nodal forces, $\mathbf{F}_{inta}^{(e)}$ and $\mathbf{F}_{exta}^{(e)}$, respectively:

$$\delta W^{(e)} = \delta\mathbf{u}_a \cdot \left( \int_{V(e)} \boldsymbol{\sigma} N_a dV - \int_{V(e)} N_a \mathbf{f} dV - \int_{S_2^{(e)}} N_a \mathbf{t} dA \right) = \delta\mathbf{u}_a \cdot \left( \mathbf{F}_{inta}^{(e)} - \mathbf{F}_{exta}^{(e)} \right) \tag{3.65}$$

where $\mathbf{F}_{\text{int a}}^{(e)} = \int_{V^{(e)}} \boldsymbol{\sigma} N_a dV$ and $\mathbf{F}_{exta}^{(e)} = \int_{V^{(e)}} N_a \mathbf{f} dV - \int_{S_2^{(e)}} N_a \mathbf{t} dA$.

Since the virtual work equation must be satisfied for any arbitrary virtual displacement and the equilibrium conditions require that $\delta W^e = 0$, the discretized equilibrium equations, in terms of nodal residual force $\mathbf{R}_{fa}^{(e)}$, emerges as:

$$\mathbf{R}_{fa}^{(e)} = \left( \mathbf{F}_{inta}^{(e)} - \mathbf{F}_{exta}^{(e)} \right) = 0 \tag{3.66}$$

After summing the contribution of every node and element (the assembling process), the global equilibrium equation in the discretized form may be written as:

$$\mathbf{R}_f = (\mathbf{F}_{inta} - \mathbf{F}_{ext}) = 0 \tag{3.67}$$

### 3.5.2 Linearization of the Principle of Virtual Work

The principle of virtual work, previously presented, can be linearized, considering a trial solution $\varphi_k$, in the direction of an increment $\Delta\mathbf{u}$ in $\Phi_k$ as [39]:

$$\delta W\left(\varphi_k, \delta\mathbf{u}\right) + D_{\Delta\mathbf{u}}\delta W\left(\varphi_k, \delta\mathbf{u}\right) = 0 \tag{3.68}$$

where the operator $D$ is the directional derivative of the virtual work equation at $\varphi_k$ in the direction of $\Delta\mathbf{u}$. Thus, to bring the internal forces into equilibrium with the external forces, following the Newton-Raphson procedure, the configuration $\varphi_k$ must be adjusted. The linearization of the equilibrium equation [39] will be considered in terms of internal and external work components as:

$$D_{\Delta\mathrm{u}}\delta W\left(\varphi_k, \delta\mathrm{u}\right) = D_{\Delta\mathrm{u}}\delta W_{int}\left(\varphi_k, \delta\mathrm{u}\right) - D_{\Delta\mathrm{u}}\delta W_{ext}\left(\varphi_k, \delta\mathrm{u}\right) = 0 \tag{3.69}$$

Regardless of the complexity of the definition of the directional derivate, the final expression's discretized form may be expressed as follows:

$$D_{\Delta\mathbf{u}}\delta W\left(\varphi_k, \delta\mathbf{u}\right) = \delta\mathbf{u}^T\mathbf{K}\mathbf{u} \tag{3.70}$$

where $\mathbf{K} = \frac{\partial\Delta\boldsymbol{\sigma}}{\partial\Delta\boldsymbol{\varepsilon}}$ corresponds to the stiffness matrix.

Considering equation 3.67, and substituting equation 3.70 into equation 3.68:

$$\mathbf{R}_f + \mathbf{K}\mathbf{u} = 0 \tag{3.71}$$

which provides the basis of the iterative Newton-Raphson scheme, that can be formulated as:

$$\mathbf{K}\mathbf{u} = -\mathbf{R}_f\left(x_k\right); \quad x_{k+1} = x_k + \mathbf{u} \tag{3.72}$$

### 3.5.3 ABAQUS® Finite Element Software

ABAQUS® is a finite element analysis and computer-aided engineering software. Based on the finite element method, it is capable of solving different types of problems ranging from simple linear analysis to the most challenging nonlinear simulations. Consisting in a vast product set, it includes ABAQUS/CAE® (Complete ABAQUS® Environment) - is used for the modeling and analysis of mechanical components and assemblies, as well as to visualize the finite element analysis result - and ABAQUS/Standard® - a general-purpose analysis product that can solve a wide range of linear and nonlinear problems. The software offers an extensive library of elements and the most common materials already defined. For complex problems, it enables the development of a user subroutine, known as UMAT, to consider specific constitutive equations to calculate the stiffness matrix and the stresses.

# Chapter 4
# Finite Element Simulations

## 4.1 Introduction

In this chapter the main practical work takes place. Through the enumeration of the potentially most accurate constitutive models, the reader may find all the information that leads to the best approximation for the filaments and meshes properties. Keeping in mind the computationally assisted procedure, all the simulations feature similar conditions to the ones imposed during the experimental tests [41].

As a first step, relying on the existence of trustful data from previous experiments [29], a traditional approach took place with the purpose of verifying PCL's mechanical properties. Thus, for the ultimate goal of properly evaluating and designing software based mesh models, matching the stress-strain curve from the experiments with a similar performance, an appropriate constitute model for different diameters of PCL filaments was needed. As for the second step, once again keeping in mind the availability of previous examples, computational simulations were also put into motion, subjecting the mesh models to displacement and encastre boundary conditions. This time, after having found the best model to approximate the filaments' properties, the simulations were made with that very model. The procedure was repeated on different mesh geometries in order to understand which would favour a better performance for the implants. Table 4.1 lists the several steps involved in a finite element analysis.

| Steps | Description |
|---|---|
| *1* | Dicretizing the structure. The continuum body is subdivided in finite elements - segments - with the creation of the mesh. |
| *2* | Connecting the several elements by a discrete number of nodal points called nodes. |
| *3* | Defining of the elements' material properties. |
| *4* | A set of functions is chosen in order to define the nodal displacement of each node. |
| *5* | The displacement functions dictate the strain magnitude which, together with the constitutive law of the material, defines the stress magnitude. |
| *6* | The stiffness, damping and inertial matrices create the relationship between the nodal displacements, velocity and acceleration exerted in the nodes. |
| *7* | Applying external loads and torques. |
| *8* | Defining boundary conditions. |
| *9* | Solving algebraic equation systems. |
| *10* | Calculating displacement, stress or reaction values. |

Table 4.1: Steps in FEM structural analysis (adapted from [1]).

## 4.2 Constitutive Models

A material's constitutive law is expressed by the relationship between stress and strain, being related to the Poisson coefficient and the Young modulus for linear elastic materials and given by the strain potential energy in the case of hyperelastic materials – Equation 4.1. This section aims at the description of such models, as a theoretical baseline for understanding the computational assistance provided by Abaqus, before moving to the filament and mesh modelling. It is important to point out the fact that the whole procedure starts at the point where PCL is defined and, consequently, its properties and mechanical behaviour.

$$U = \sum_{i+j=1}^{N} C_{ij} \left(\bar{I}_1 - 3\right)^i \left(\bar{I}_2 - 3\right)^j + \sum_{i=1}^{N} \frac{1}{D_i} \left(J_{el} - 1\right)^{2j} \tag{4.1}$$

In the previous expression, $J_{el}$ is the elastic volume ratio, whereas $\bar{I}_1$ and $\bar{I}_2$ measure the material distortion. The parameters $N$, $C_{ij}$ e $D_i$ may be temperature dependent; the second relates to the shear behaviour of the material and the third is a compressibility quantity.

### 4.2.1 Linear Elastic

For linear elastic materials that are exposed to uniaxial tension, as stated before, only the Young modulus is needed to express the relationship between stress and strain. The constitutive law is shown in Equation 4.2.

$$\sigma = E\varepsilon \tag{4.2}$$

Here, $\sigma$ is the stress associated with a strain $\varepsilon$ and defined by the material stiffness represented by N. It is important to notice that permanent deformation occurs beyond the elastic limit. However, for the case of the current work, the simulations took in consideration the behaviour until that limit only.

### 4.2.2 Hyperelastic

#### 4.2.2.1 Neo-Hookean

This model is given by the following equation:

$$U = C_{10} \left(\bar{I}_1 - 3\right) + \frac{1}{D_1} \left(J^{el} - 1\right)^2 \tag{4.3}$$

Here, **U** represents the strain potential energy per unit volume. The coefficients $C_{10}$ and $D_1$ define two temperature dependent parameters of the material and $\bar{I}_1$ the first invariant of the deflection strain tensor given by $\bar{I}_1 = \bar{\lambda}_1^2 + \bar{\lambda}_2^2 + \bar{\lambda}_3^2$. The parameter $\bar{\lambda}_i$ represents the *deviatoric stretches* and it is given by $\bar{\lambda}_i = J^{-\frac{1}{3}} \lambda_i$, being $\lambda_i$ the first *main stretch* [42].

#### 4.2.2.2 Yeoh

The Yeoh model is given by equation 4.4.

$$U = C_{10}\left(\bar{I}_1 - 3\right) + C_{20}\left(\bar{I}_1 - 3\right)^2 + C_{30}\left(\bar{I}_1 - 3\right)^3 + \frac{1}{D_1}\left(J^{el} - 1\right)^2 + \frac{1}{D_2}\left(J^{el} - 1\right)^4 + \frac{1}{D_3}\left(J^{el} - 1\right)^6 \tag{4.4}$$

Where $C_{i0}$ and $D_i$ are two temperature dependent parameters of the material and $\bar{I}_i$ represents the invariant of the deflection strain tensor [42].

## 4.3 Filaments

Previous analyses have studied the efficacy of commercial synthetic pelvic implants as a function of the attachment point for mesh anchorage [8], as well as their adequacy for different degrees of tissue impairment [43]. For both cases various constitutive models were applied in order to address the mechanical behaviour of the implants - Yeoh and Ogden hyperelastic are two examples [43]. For these commercial implants, the well-known properties of the synthetic material assured a better performance of the meshes due to the fact that prototypes could be tested and adjusted during the development phase. The main goal of the current work has been to extend those capabilities to cases with new and improved materials, such as PCL, that may offer a more appropriate solution for treating POP.

Starting with the filaments, there were two values for the diameter. Each one was a reference from the experimental data so all the models were simulated for both diameters as well: one measuring 160 micrometers, with a cross-sectional area of 0.02 square millimeters and the other 240, with a cross-sectional area of 0.04524 square millimeters. According to the experimental data, the samples' initial length of 50 millimetres was extended in 30% by displacing one end of the filament and fixating the other as an encastre support. Even though the measurements included the plastic deformation zone, the goal was to monitor the material's behaviour until the elastic limit stress point, once this is the strain range on which the mesh implants are meant to function – avoiding permanent deformation.

As described in the previous section, two options were considered for the material characterization. The first – to define the polymer as a linear elastic material – implied the selection of a specific point within the linear part of the stress-strain curve so that the stiffness could be determined. For the second option, regarding the hyperelastic approximation, a primary material evaluation was made to get a first set of constitutive models, capable of properly matching the measured performance. Figure 4.1 shows the resulting data points extracted from the tensile tests on PCL filaments, carried out with samples of both diameters and, consequently, the limit of the elastic regime that sits at 6.5% and 10% deformation over the initial length of the 160 micrometers and the 240 micrometers filaments, respectively.

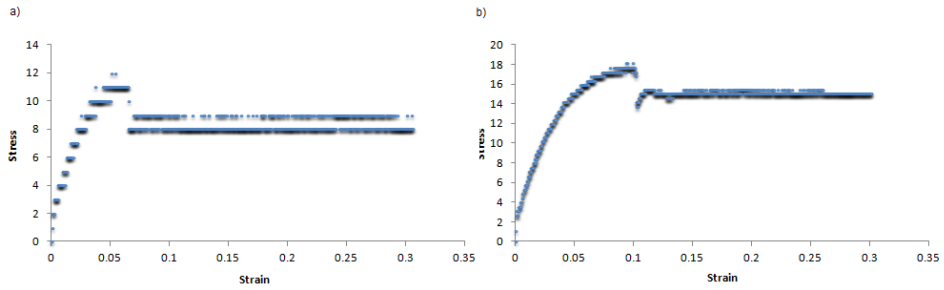


Figure 4.1: Uniaxial stress-strain response in MPa for a) a 160 micrometers PCL filament and b) a 240 micrometers PCL filament.

### 4.3.1 Young's Modulus

Within the first option of assuming a linear relationship between stress and strain for the filaments, two distinct paths could be followed. The first relates to the theoretical value of PCL Young's Modulus. According to the literature [44], it can range between 343.9 and 363.4 MPa and the Poisson coefficient sits at 0.3 – value used in all of the linear analyses in the current work. Thus, for the lower and upper limit of this interval and relying on Equation 4.2, the stress associated with the maximum strain – for the elastic limit reference – was calculated. This procedure would lead to an approximation of the real stress-strain curve or, at least, to the invalidation of using this theoretical value as a reference.

However, the mechanical properties of the extruded material could differ from the ones stated by the literature, especially because a material's behaviour like the one studied here is expected to change depending on the geometry of the sample – on the filament's diameter, in this case. This hypothesis would invalidate these references and its existence was actually the very first motivation for this problem to be addressed in the current work – aiming at a proper understanding of 3D printed fibers of PCL. In order to extract the experimental Young's Modulus, the previously mentioned limit point of deformation – 3.238 and 5.073 millimetres for the 160 and 240 micrometres samples, respectively – would provide both the stress and the strain to be used in Equation 4.2. From here, further conclusions on the disparity between the theoretical and the experimental values for the Young's Modulus would be taken, also giving meaning to the change in stiffness as a function of the filament section. Nevertheless, it is crucial to notice the fact that this approach leads only to a close estimate once the curve is not perfectly linear.

### 4.3.2 Simulation Procedure

Regarding the finite element simulations developed in ABAQUS ®, and considering the intention to reproduce a uniaxial tensile test, beam elements stood as the best option to simulate the filaments which were represented as

wires. Once the measured stresses and strains manifest only in the direction of the displacement – X direction – and the stress is constant across the filament's length, a single element per beam would assure a precise simulation. From here, the boundary conditions were defined as static, applying the mentioned displacement on one end of each filament – since that was a safe reference for the end of the elastic regime for both samples – and an encastre support on the other. Figure 4.2 shows these configurations with a print from an ABAQUS ® file. After submitting the analysis, the results would offer stress values that, determined by the described simulation specificities, could point to the most adequate constitutive model, according to the experimental data.


Figure 4.2: Boundary conditions representation for a filament model.

It is important to mention the contrast between the linear elastic and the hyperelastic simulations. Considering it would all come down to the way the material is defined, once the circumstances of the tensile test are constant, the first case presented itself as a simpler, more direct replication of the material properties – the previous topic "Young's Modulus" explains it. As for the second case, the experimental data displayed on Tables 4.2 and 4.3 was introduced in the software so that the constitutive equations could find the required parameters to adjust to each given curve. Using experimental data points is an alternative to the procedure of the linear elastic case, where the material's properties where manually introduced and defined its behaviour.

### 4.3.3 Model Parameters

Regardless of the fact that the use of experimental data points does not depend on previously defining the parameters for the constitutive equations, ABAQUS® creates them after simulations are submitted. This outcome, allied with the resulting stress values, is an indicator of how close the simulation comes to real behaviour of the samples. This iterative process – repeating the analysis with the new coefficients and gauging them – enables the understanding of how these parameters affect the veracity of the approximation and allows the user to implement them in further analyses – namely with the mesh models. The procedure stands as similar to the one developed on the linear

Table 4.2: Stress-Strain data points from the uniaxial tensile test developed on the 160 micrometres diameter sample.

| **Nominal Strain** [standard travel/initial length] | **Nominal Stress** [MPa] |
|---|---|
| 0 | 0 |
| 0.00050354 | 0.7624 |
| 0.0015881 | 1.4625 |
| 0.00455127 | 2.2475 |
| 0.00722392 | 3.118 |
| 0.00939304 | 3.837 |
| 0.01342139 | 4.218 |
| 0.01477709 | 5.256 |
| 0.01987063 | 6.142 |
| 0.02196227 | 6.925 |
| 0.02728822 | 7.542 |
| 0.03116164 | 8.396 |
| 0.03639075 | 9.265 |
| 0.04599682 | 10.15625 |
| 0.05837239 | 10.894 |
| 0.06162606 | 11.71875 |
| 0.06271062 | 12.05 |

Table 4.3: Stress-Strain data points from the uniaxial tensile test developed on the 240 micrometres diameter sample.

| **Nominal Strain** [standard travel/initial length] | **Nominal Stress** [MPa] |
|---|---|
| 0 | 0 |
| 0.00054161 | 1.4532739 |
| 0.00247891 | 3.60504764 |
| 0.0057494 | 4.544051 |
| 0.00772836 | 5.64570242 |
| 0.01029059 | 6.5946433 |
| 0.0150401 | 7.59822624 |
| 0.01939381 | 8.35075006 |
| 0.0239975 | 10.468293 |
| 0.02837204 | 11.6274048 |
| 0.03385064 | 12.452817 |
| 0.03962087 | 14.0320596 |
| 0.04557859 | 15.483215 |
| 0.0601604 | 16.764814 |
| 0.07101344 | 17.4859863 |
| 0.0802833 | 17.76073 |
| 0.10425997 | 18.118692 |

elastic model since the simulation does not rely on experimental data points to model the samples behaviour, only on input values.

Apart from these considerations related to the linear elastic and hyperelastic properties, which were properly attributed to the 50 millimetres long wire, the sections were also defined as circular, according to the experimental samples.

## 4.4 Meshes

For the development of the mesh models, two geometries had also been previously tested, having been built with the two filament samples. This experimental data, comparatively to the one used as the filaments' properties source, plays the role of referencing the parameters measured during the unaxial tensile tests with the meshes, as well as of serving as a term of comparison within the comfort zone - once placed, the implants' behaviour is divided in two areas, according to how their strain feels to the patient, and the comfort zone extends up to 13% deformation. These two geometries represent a starting point in terms of mesh implant design as further improvements shall be necessary for a better reproduction of natural tissue properties. Still, since these samples materialize a new concept for the manufacturing of such products, their intuitive design enables the depiction of the nuances to be taken into account in cases where melt-electrospinning writing is the production technique. The two patterns may be seen in Figure 4.3 through an ABAQUS® representation.

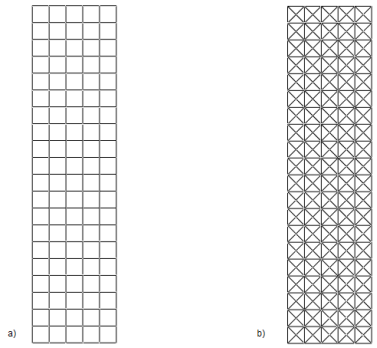


Figure 4.3: Software based representation of the mesh models: a) square-shaped mesh; b) cross-shaped mesh.

Like in the filament analysis, these simulations had to be developed for two different thickness values – both geometries were simulated with a 160 micrometers diameter section and a 240 micrometers diameter section. According to the experimental data, the samples' initial length of 40 millimetres was extended in 25% by displacing one end of the filament and fixating the other as an encastre support. With the filaments the extension imposed during the experiments had forced the material into the plastic deformation regime

(during the experiments), and the same happened with the meshes, hence the simulations being developed inside the comfort zone where only linear elastic behaviour is witnessed. The goal was to study the meshes inside the elastic regime, avoiding permanent deformation on the implants.

For this part of the work, the material would then be defined as linear elastic once this was the model that best suited the experimental data during the filaments' simulations. Even though two different diameters were in play, the used Young's Modulus did not differ as a function of this factor. For the two diameter values disposed according to the square-shaped mesh geometry, Figure 4.4 is a graphic representation of the experimental data, being important to acknowledge the resemblance between the mesh behaviour and the filament behaviour (linear elastic) up to a 10% elongation for the meshes built with 160 micrometers diameter filaments and 240 micrometers diameter filaments, respectively. Consequently, the associated Young's Modulus was measured in these points.

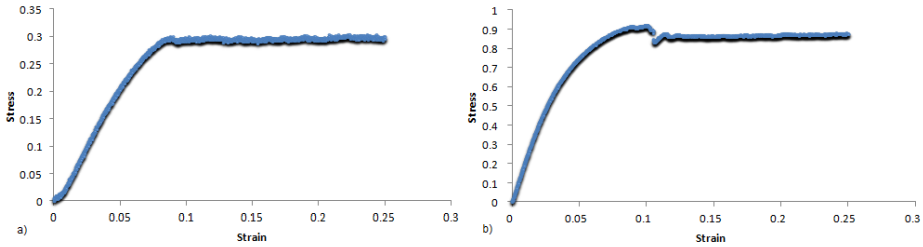


Figure 4.4: Uniaxial stress-strain response in MPa for a) a 160 micrometers PCL filament square-shaped mesh and b) a 240 micrometers PCL filament square-shaped mesh.

Similarly, for the cross-shaped mesh, Figure 4.5 shows the experimental data. The interval of linear elastic behaviour was, for the case of this geometry, assumed up to a 7.5% elongation. Consequently, the structures Young's Modulus was measured in these points for both diameters.

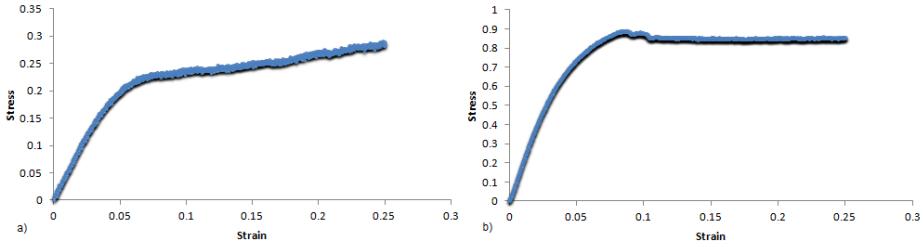


Figure 4.5: Uniaxial stress-strain response in MPa for a) a 160 micrometers PCL filament cross-shaped mesh and b) a 240 micrometers PCL filament cross-shaped mesh.

### 4.4.1 Mesh Design

As may be perceived from Figure 4.3, both geometries were developed according to the dimensions of the tested prototypes - structures with a length of 40 millimetres and a width of 10 millimetres. In spite of the fact that the printed meshes most likely presented spots of overlapped material – node points – the sections were defined evenly for both diameter values, which represented the thickness of each mesh. Comparatively to the design of the filaments, and once they may be seen as the unit measure or basic element for the several geometries, beam elements were also used to simulate the filaments, forming a net of wires that composed the final structure.

The fundamental feature of this mesh design has been the pore size replication. The printed and posteriorly tested mesh prototypes were projected with a pore size of 2 millimetres once the implants must allow natural tissue to grow in between and around them. Consequently, the models replicated with ABAQUS® should be developed accordingly. As may easily be seen with the square-shaped mesh representation in Figure 4.3, the distance between the vertical and horizontal is defined by that exact pore size of 2 millimetres.

### 4.4.2 Simulation Procedure

Aligned with the procedure exercised in the filament's analyses, the simulations for this part of the current work also aimed at reproducing the uniaxial tensile tests. The main contrast between the two is the fact that, for the meshes, the displacement is vertically applied and thus represented in the Y direction. Moreover, the chosen value for the element type was equivalent to 0.5 millimetres on behalf of the output results' reliability. The graphic practical implications of this parameter may be seen in Figure 4.6 with a representation of several nodes within a single cell of the cross-shaped mesh.

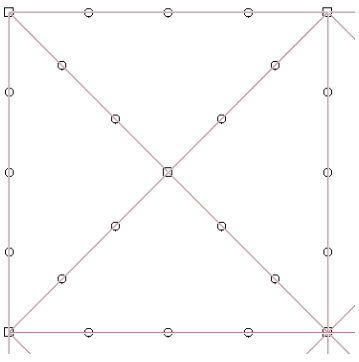

Figure 4.6: Element type used on both geometries, here represented through a 4 square millimetres cell of the cross-shaped mesh.

The boundary conditions, were also defined as static, applying a displacement on one end of the mesh – 5.2 millimetres that represents a 13% elongation - and an encastre support on the other. The 13% elongation strain

Table 4.4: High and Low Young's Modulus values in MPa for each geometry, extracted from uniaxial tensile tests applied to 3D printed mesh prototypes.

| | **Square-shaped** | | **Cross-shaped** | |
|---|---|---|---|---|
| **Diameter [$\mu$m]** | 160 | 240 | 160 | 240 |
| *Young's Modulus* | 2.98 | 9.18 | 3.04 | 8.44 |

assures the whole comfort zone will be covered, which is the main goal of the current work.

Figure 4.7 shows these configurations with a print from an ABAQUS ® file. After submitting the analysis, the results would offer stress values that, determined by the described simulation specificities, would point to the relevance of these approximations through the Linear Elastic model. Depending on the diameter, each simulation was firstly carried out relying on the Young's Modulus values previously registered. Once the circular section was properly defined, attributing it the created profile and assigning it to the mesh part, simulations were put into motion for the two cases – 160 and 240 micrometres diameter samples with the results from the filaments' simulations, a Young's Modulus of 186 MPa.

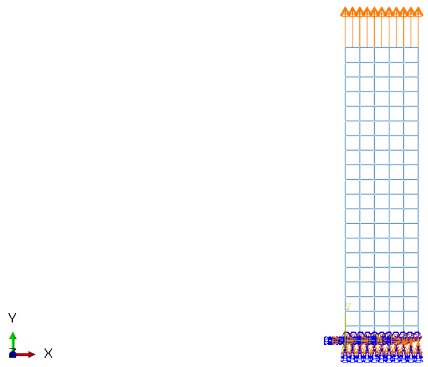


Figure 4.7: Boundary conditions representation for the square-shaped mesh.

Besides using the stiffness values obtained from the filaments' simulations, all the geometries, composed by filaments of each diameter, were simulated with the associated Young's Modulus - previously mentioned measurements at 10% and 7.5% elongation for the square-shaped and the cross-shaped geometries, respectively, regarding Figures 4.4 and 4.5. These experimental values were extracted from the experimental stress-strain curves and relate to the end of the elastic behaviour. Even though the stress-strain curve of the meshes is not perfectly linear, a good approximation up to this point was expected. Table 4.4 shows the extracted Young's Modulus values, for each geometry and diameter, assuming the meshes as an uniform sheet-like body.

# Chapter 5
# Results and Discussion

After developing the computational models described in the previous chapter, the analyses provided an insight over the problem of finding an adequate constitutive model for the replication of the filaments behaviour. Moreover, as answers were found, the meshes were also addressed in order to ultimately compare them with the stress over strain response of the Restorelle® commercial mesh and the vaginal tissue. Thus, the current chapter aims at an enumeration of the several simulations' outputs, accompanied by a detailed discussion on their relevance and accuracy. These explanations are of great importance before moving into the final conclusions of the current work. Once again, there is an inherent connection between the results of the filaments' simulations and the strategies used to model the various mesh geometries.

## 5.1 Filaments

The analyses of the procedures described above were fundamentally supported by the comparison of the stress results shown for each case – diameter and constitutive model – to the experimental values. As the reader may recall, the simulations were conducted with the intention of matching the mechanical behaviour shown on the uniaxial tensile tests. Consequently, given the clarity of the reference values, a relative error - that may be found on Table 5.1 - was calculated for each model in order to assess the best option to work with filament models inside the software. This option would be implemented in the mesh simulations afterwards.

### 5.1.1 Stress Values

The linear elastic modelling of the filaments showed interesting results. These may be seen in the following pictures 5.1 and 5.2, for the 160 and 240 micrometres diameter samples, respectively.

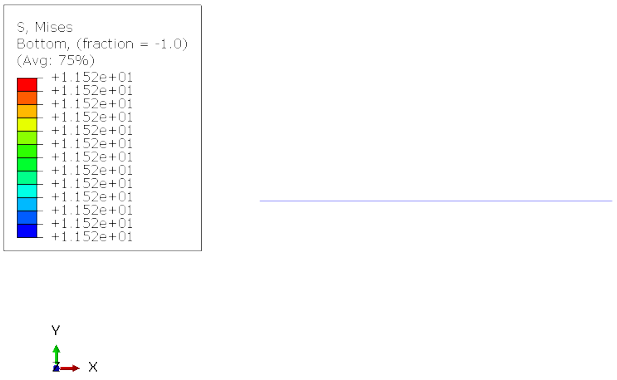


Figure 5.1: Stress value in MPa achieved by the Linear Elastic constitutive model for the 160 micrometre diameter filament.

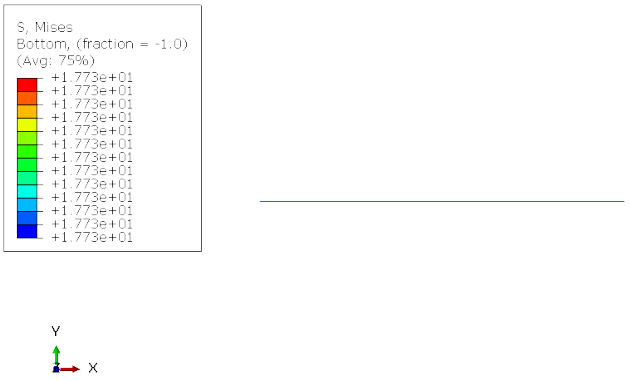


Figure 5.2: Stress value in MPa achieved by the Linear Elastic constitutive model for the 240 micrometre diameter filament.

For the Neo-Hookean constitutive model, the simulations based on the available experimental data culminated in the results presented in Figures 5.3 and 5.4 for the 160 and 240 micrometres diameter samples, respectively.

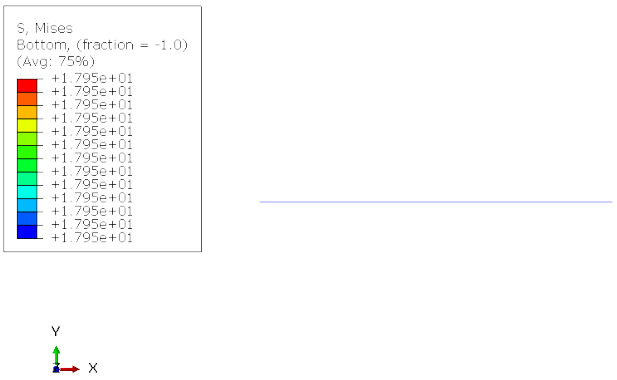


Figure 5.3: Stress value in MPa achieved by the Neo-Hookean constitutive model for the 160 micrometre diameter filament.

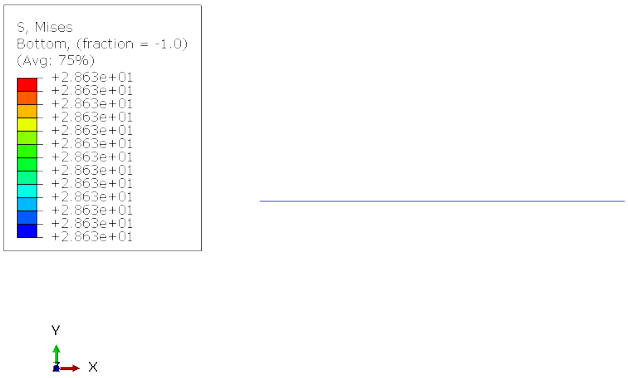


Figure 5.4: Stress value in MPa achieved by the Neo-Hookean constitutive model for the 240 micrometre diameter filament.

For the Yeoh constitutive model the results are presented in figures 5.5 and 5.6 for the 160 and 240 micrometres diameter samples, respectively.

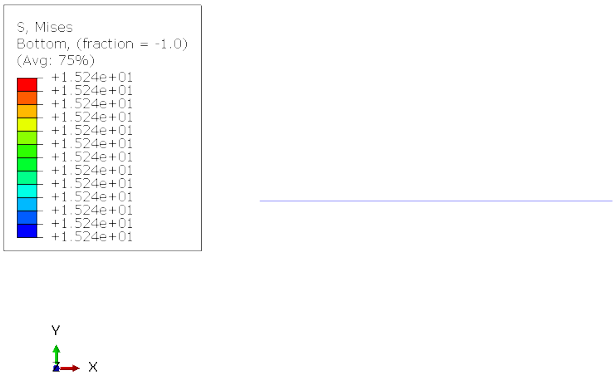


Figure 5.5: Stress value in MPa achieved by the Yeoh constitutive model for the 160 micrometre diameter filament.

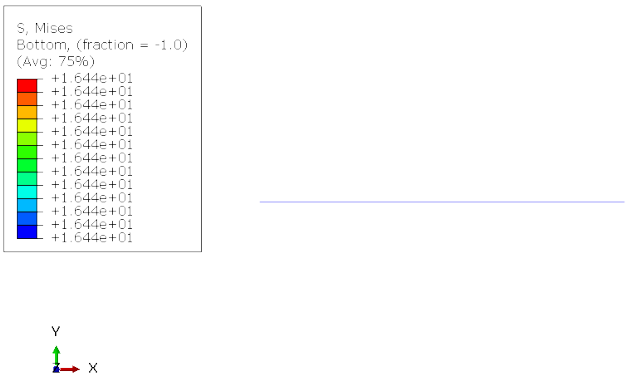


Figure 5.6: Stress value in MPa achieved by the Yeoh constitutive model for the 240 micrometre diameter filament.

### 5.1.2 Discussion

With access to the stress outputs as a function of the applied constitutive equations, it was now possible to understand which one lead to the best estimate. Starting with the linear elastic model (Poisson coefficient of 0.3) and the Young's Modulus value provided by the literature, the expected stress value was between 21.28 and 22.49 MPa for the 160 micrometres diameter sample (160) and between 34.91 and 36.89 MPa for the 240 micrometres diameter sample (240). Knowing that the registered values during the tensile tests were 12.05 and 18.12 MPa for the 160 and 240, respectively, it is safe to assume that the properties of the 3D printed PCL are considerably different to the ones mentioned by the literature. This is most likely linked to the high temperatures of extrusion associated with the melt electrospining writing, as well as to the time associated with the cooling of the materials. These factors imply physical transformations that alter the stiffness and, consequently, the elastic behaviour of the polymer.

For the case where the Young's Modulus was extracted from the experimental data, its value was of 186 MPa. The previously shown output stresses may be taken as accurate simulations since their values fell at 11.52 and 17.73 MPa for the 160 and 240 filaments, respectively. This outcome is not surprising once the reference data point was in fact the limit value of the elastic regime. Plus, once the simulations aimed at mimicking the experimental tests, the conformity between the results was predictable; in order to match a linear segment of a stress-strain curve, the material shall be defined as linear elastic.

Table 5.1: Stress values extracted from the simulations made with different constitutive models; Relative error of each measurement according to the uniaxial tensile test experimental data.

| | **160 $\mu$m** | | **240 $\mu$m** | |
|---|---|---|---|---|
| | **Stress [MPa]** | **error [%]** | **Stress [MPa]** | **error [%]** |
| **Experimental Data** | 12.05 | n/a | 18.12 | n/a |
| Literature Values | 21.28-22.49 | 70-79 | 34.91-36.89 | 126-139 |
| Linear Elastic | 11.52 | 4.4 | 17.73 | 2.2 |
| Yeoh | 15.24 | 26.5 | 16.44 | 9.3 |
| Neo-Hookean | 17.95 | 49 | 28.63 | 58 |

For this comment section to be concluded, the hyperelastic constitutive models must also be questioned. Since the tested 3D printed PCL is not characterized by a perfectly linear elastic regime, it was reasonable to register the coefficients of the constitutive equations from the Yeoh model - Figures 5.7 and 5.8 show them for both diameters. These were not registered for the Neo-Hookean model as the discrepancy between the output stresses of this constitutive equation and the experimental stress data clearly indicates the inadequacy of using it to simulate the PCL filaments.

Considering the values of the relative error presented in Table 5.1, the Neo-Hookean model was discarded promptly. The predictions made by this

model were far worse than the ones achieved by the linear elastic model. As for the Yeoh constitutive models, despite the associated errors being lower than the ones of the Neo-Hookean model, the Linear Elastic model still represents the best option for modelling the 3D printed material

HYPERELASTICITY - POLYNOMIAL STRAIN ENERGY FUNCTION WITH N = 3

| D1 | C10 | C01 | | |
|---|---|---|---|---|
| D2 | C20 | C11 | C02 | |
| D3 | C30 | C21 | C12 | C03 |
| 0.00000000 | 73.4385621 | 0.00000000 | | |
| 0.00000000 | -5148.68943 | 0.00000000 | 0.00000000 | |
| 0.00000000 | 205965.639 | 0.00000000 | 0.00000000 | 0.00000000 |

Figure 5.7: Extracted parameters from the Yeoh constitutive model simulation for the 160 micrometre diameter filament.

HYPERELASTICITY - POLYNOMIAL STRAIN ENERGY FUNCTION WITH N = 3

| D1 | C10 | C01 | | |
|---|---|---|---|---|
| D2 | C20 | C11 | C02 | |
| D3 | C30 | C21 | C12 | C03 |
| 0.00000000 | 82.24616955 | 0.00000000 | | |
| 0.00000000 | -2409.11219 | 0.00000000 | 0.00000000 | |
| 0.00000000 | 33756.9659 | 0.00000000 | 0.00000000 | 0.00000000 |

Figure 5.8: Extracted parameters from the Yeoh constitutive model simulation for the 240 micrometre diameter filament.

From here, the work proceeded towards modelling and simulating the behaviour of the meshes, taking into account the Linear Elastic model. It is clear that the PCL filaments' behaviour must be defined as linear elastic in order to be simulated inside that same regime. In the first simulations, the meshes were modeled using the Young's Modulus value obtained during the filaments' simulations - 186 MPa. Even though the Yeoh model could also be an adequate option for the 240 micrometres diameter sample, the meshes composed by filaments with this section area shall also be simulated with the Linear Elastic model. Nevertheless, the experimental measurements taken from the tensile tests on mesh prototypes shall be considered as well.

## 5.2 Meshes

The presented stress distributions shall be compared considering the influence of different values for the Young's Modulus of the structures - numerical (filaments' simulations) and experimental. These representations show a gradient of stress values throughout the mesh structures that will also be compared with each other so that the influence of the geometry may be understood. Afterwards, the comparison between the stress-strain curve obtained from the simulations takes place, using the results from the experimental data registered on the uniaxial tensile tests on mesh prototypes. Similarly to the filaments' results presentation, the stress maps of the three geometries are listed and commented bellow.

### 5.2.1 Stress Values

Four simulations were made with the square-shaped geometry. Each section area was tested for a 13% elongation, given two different sources for the Young's Modulus values. The following Figures 5.9, 5.10, 5.11 and 5.12 show the taken measurements.

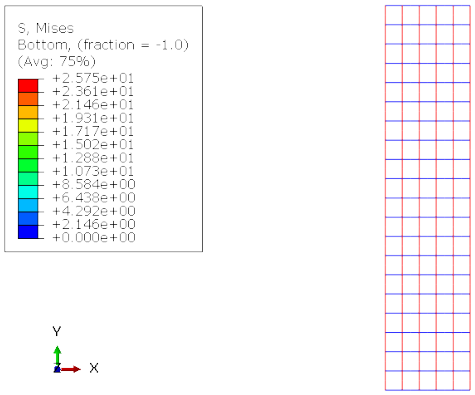


Figure 5.9: Stress distribution in MPa measured in the square-shaped mesh built with the 160 micrometre diameter filament at a 5.2 millimetre displacement; Young's Modulus = 186 MPa (measured for the filaments).

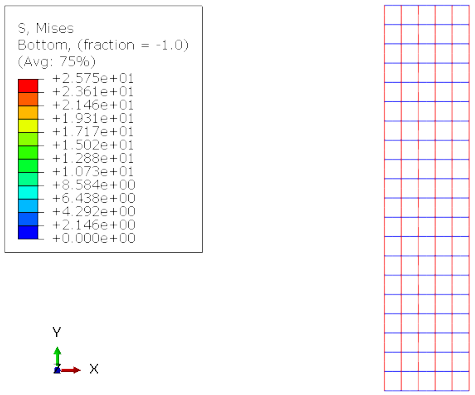


Figure 5.10: Stress distribution in MPa measured in the square-shaped mesh built with the 240 micrometre diameter filament at a 5.2 millimetre displacement.; Young's Modulus = 186 MPa (measured for the filaments).

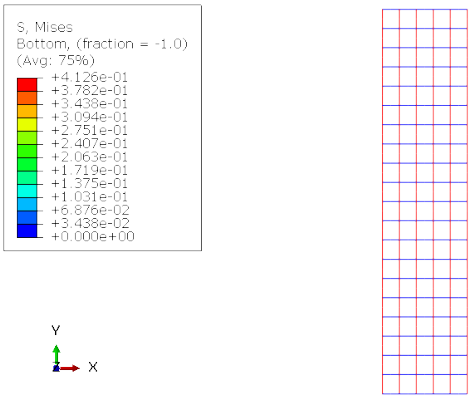


Figure 5.11: Stress distribution in MPa measured in the square-shaped mesh built with the 160 micrometre diameter filament at a 5.2 millimetre displacement.; Young's Modulus = 2.98 MPa (experimental).

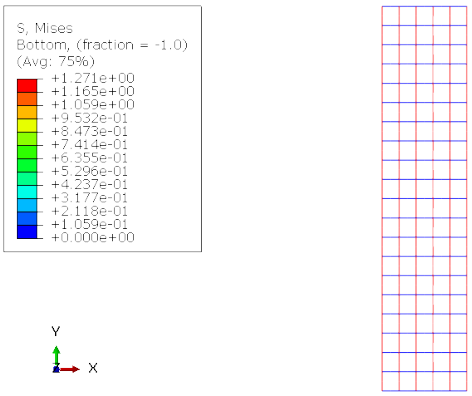


Figure 5.12: Stress distribution in MPa measured in the square-shaped mesh built with the 240 micrometre diameter filament at a 5.2 millimetre displacement.; Young's Modulus = 9.18 MPa (experimental).

As for the cross-shaped geometry mesh, both the 160 and 240 micrometres filaments were used and the four possibilities mentioned above were also put into practice. Figures 5.13, 5.14, 5.15 and 5.16 show the associated stress distributions.

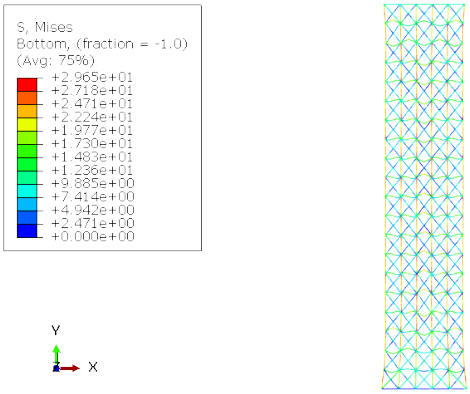


Figure 5.13: Stress distribution in MPa measured in the cross-shaped mesh built with the 160 micrometre diameter filament at a 5.2 millimetre displacement; Young's Modulus = 186 MPa (measured for the filaments).

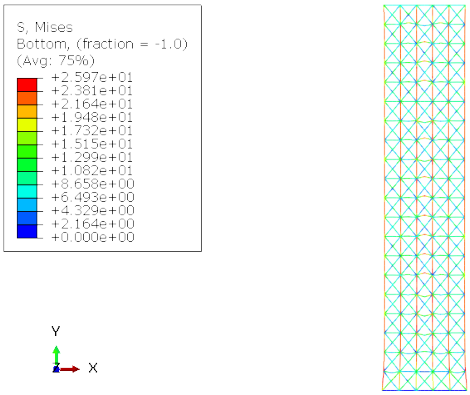


Figure 5.14: Stress distribution in MPa measured in the cross-shaped mesh built with the 240 micrometre diameter filament at a 5.2 millimetre displacement; Young's Modulus = 186 MPa (measured for the filaments).

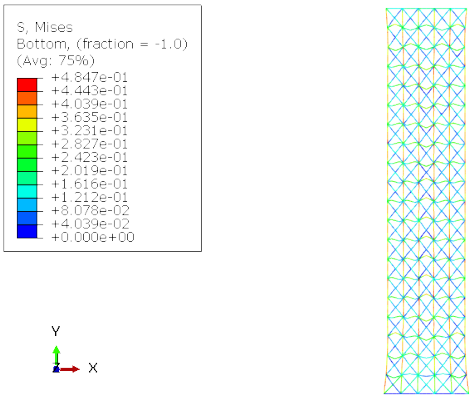


Figure 5.15: Stress distribution in MPa measured in the cross-shaped mesh built with the 160 micrometre diameter filament at a 5.2 millimetre displacement; Young's Modulus = 3.04 MPa (experimental).

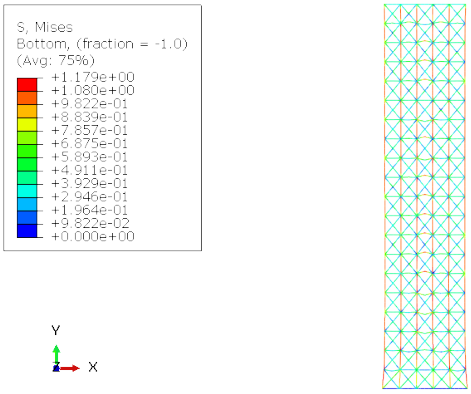


Figure 5.16: Stress distribution in MPa measured in the cross-shaped mesh built with the 240 micrometre diameter filament at a 5.2 millimetre displacement; Young's Modulus = 186 MPa (experimental).

### 5.2.2 Stress-Strain Curves

The curves are compared with the experimental ones - shown by Figures 5.17, 5.18, 5.19 and 5.20. Once the values registered on the simulations with the numerical Young's Modulus may be discarded (explained in the next subsection), the stress-strain relationship is shown only for the simulations using the stiffness value measured form the experimental data.

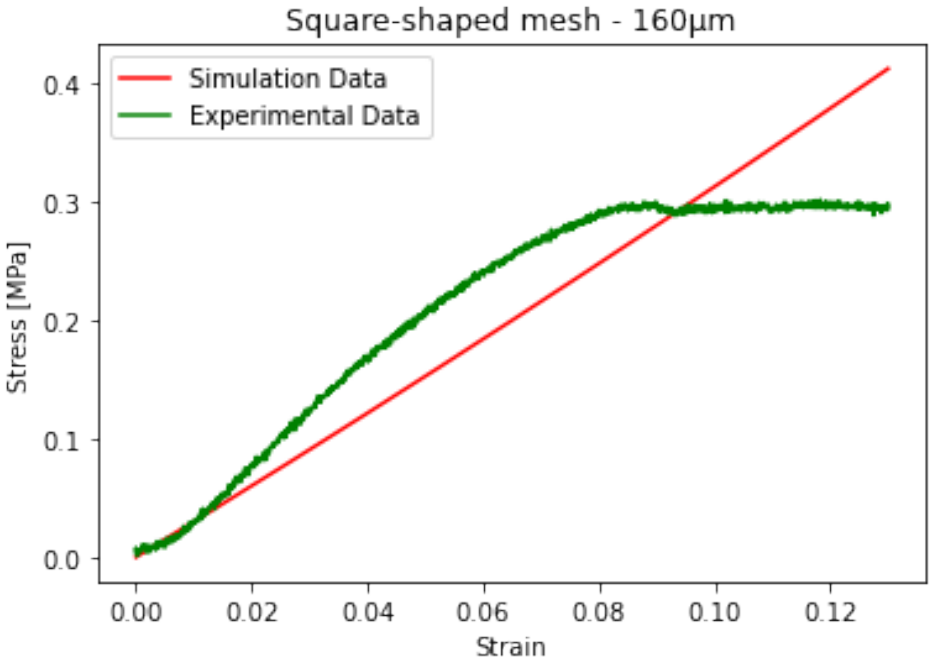


Figure 5.17: Stress-strain relationship for the square-shaped mesh built with the 160 micrometre diameter filament, up to a 5.2 millimetre displacement.

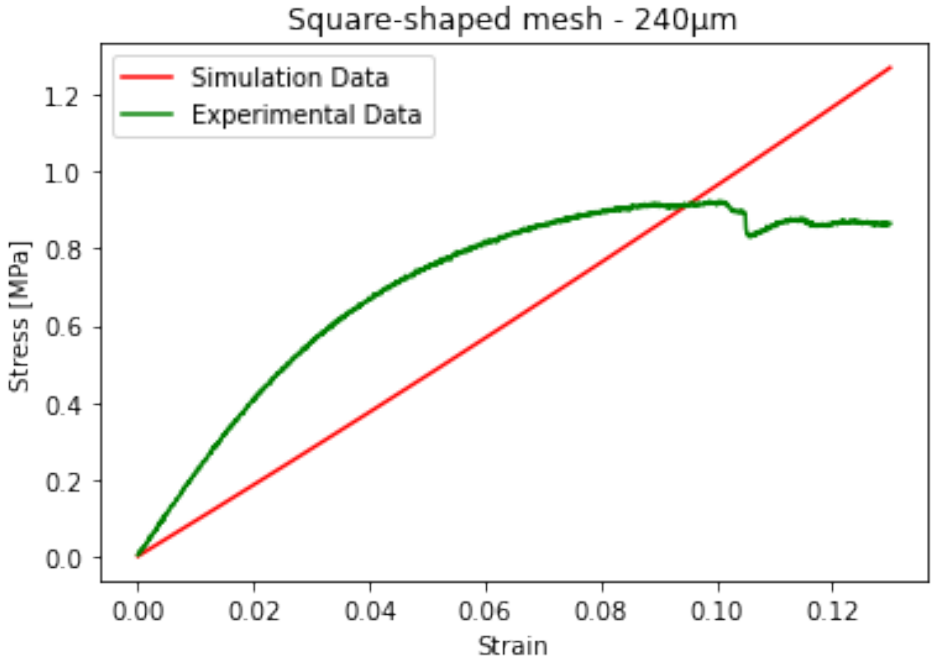


Figure 5.18: Stress-strain relationship for the square-shaped mesh built with the 240 micrometre diameter filament, up to a 5.2 millimetre displacement.

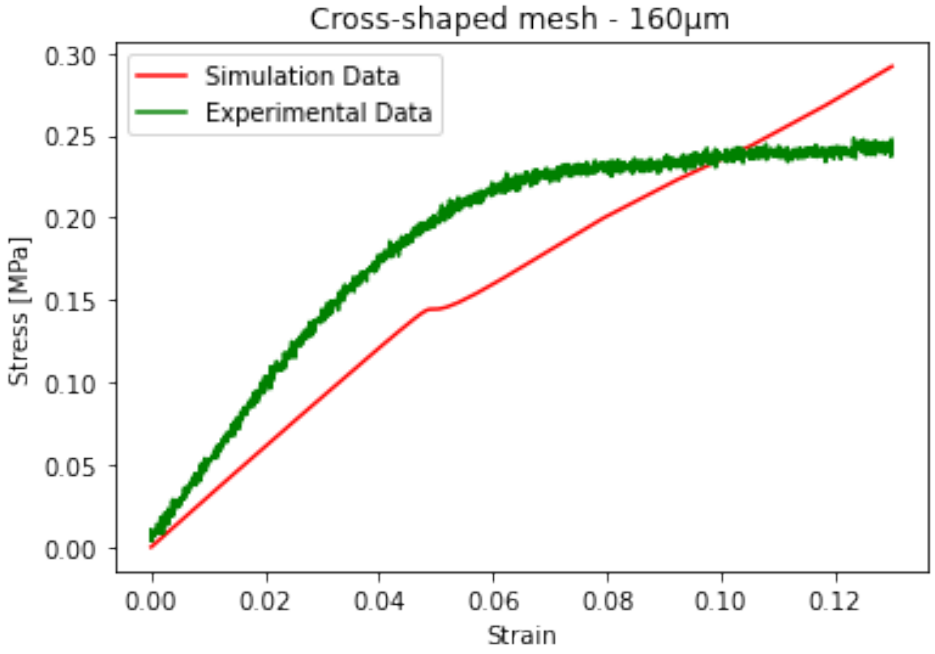


Figure 5.19: Stress-strain relationship for the cross-shaped mesh built with the 160 micrometre diameter filament, up to a 5.2 millimetre displacement.

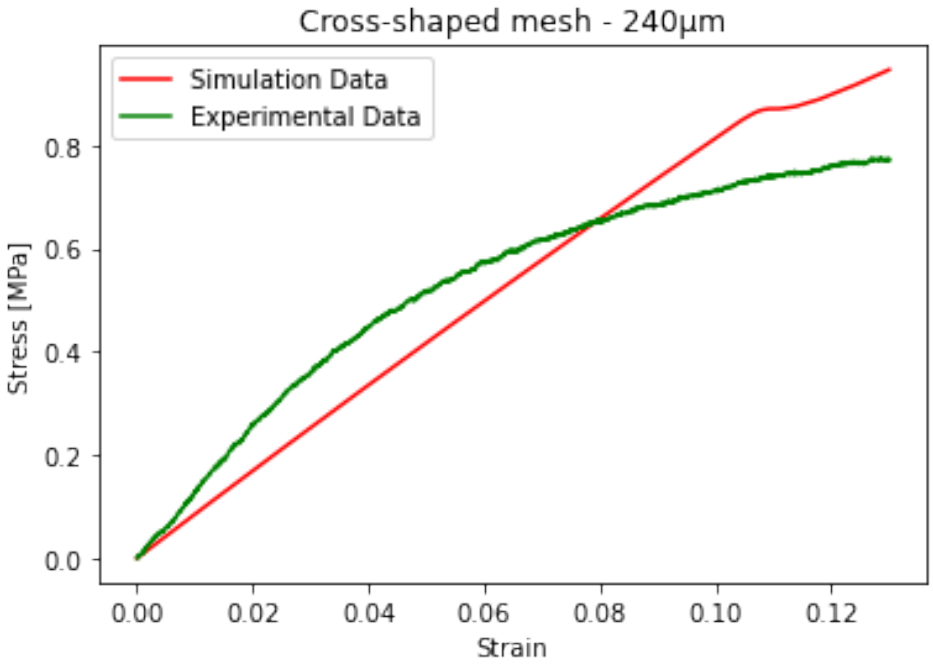


Figure 5.20: Stress-strain relationship for the cross-shaped mesh built with the 240 micrometre diameter filament, up to a 5.2 millimetre displacement.

### 5.2.3 Discussion

First of all, regarding the simulations developed with the Young's Modulus measured during the filament's simulations, the stress distributions on the computationally modeled meshes were not representative of the real stress response from the meshes during the experimental uniaxial tests. Hence the numerical stress-strain curves not featuring these cases. The reason behind this is related to the fact that the models designed in ABAQUS ® respect the geometrical characteristics of the previously printed prototypes, which implies a variable sectional area across the meshes' length and, consequently, the need for a different stiffness value to represent the whole structure.

As for the simulations run after using the experimental stress-strain response from the mesh prototypes as the source for the Young's Modulus values, the results were quite more interesting. The reader may see how the stresses are more evenly distributed with cross-shaped geometries, a detail that indicates how crucial geometry manipulation is in order to improve the surgical implants' performance. The resemblance to the experimental stress values, accordingly to what happened with the filaments, is justified by the fact that the mesh properties were thoroughly replicated in the software. An important part of these results analyses, before looking at each mesh geometry and thickness independently, is to understand that, for each one of the simulations, the stress values are only a realistic representation up to the end of the meshes' elastic regime. The first rupture points do not exist in the simulations since the models were assumed to maintain their stiffness throughout

the whole comfort zone. Nevertheless, when looking at the elastic regime, the applied strains trigger a properly matched stress response, especially for the square-shaped mesh composed by 160 micrometers diameter filaments and for the cross-shaped mesh composed by 240 micrometers diameter filaments. The square-shaped mesh geometry composed by 240 micrometres diameter filaments suggests that the linear elastic model may be too inaccurate in this case. Lastly, the cross-shaped models tend to show a higher resemblance with the experimental curves.

Finally, the curves must be compared with the ones of the Restorelle® commercial mesh and of the vaginal tissue. Figure 5.21 displays this information, like in the examples listed above, in a stress-strain graph.

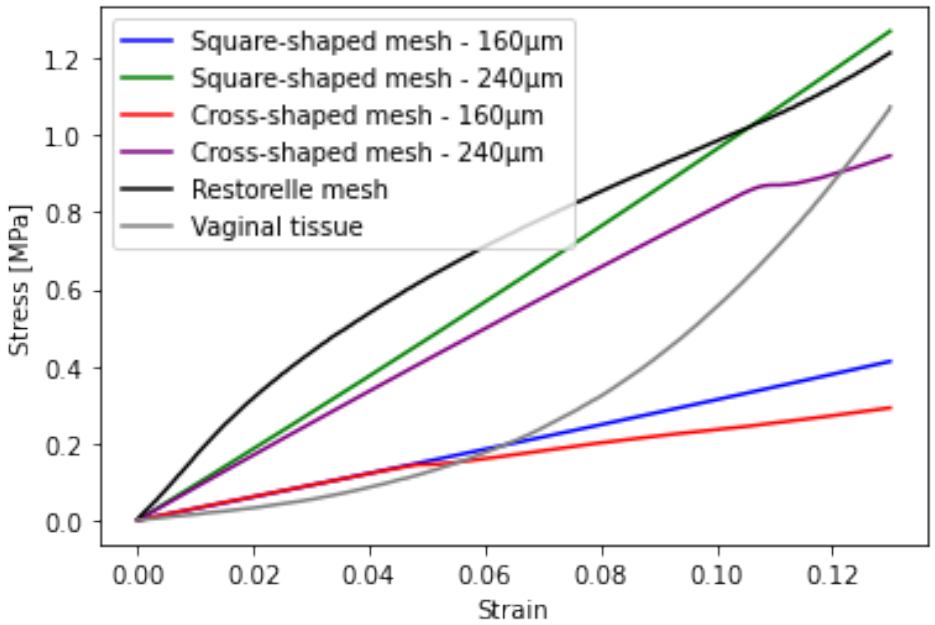


Figure 5.21: Stress-strain relationship for all meshes and the vaginal tissue.

The reader is now able to understand how the thickness - filaments' diameters - may influence the meshes stress response. It is seen that the 160 micrometres geometries perform better up to a 6% deformation, using the vaginal tissue curve as a reference. However, after this strain point, the resemblance is no longer verified. For the geometries with a 240 micrometres thickness, even though their performance is not as good for initial strain values - using the vaginal tissue curve as a reference - the second half of the graph suggests that these may actually be a better option than the Restorelle® commercial mesh since they show a lower rigidity and might, as a consequence, induce less discomfort on the patient.

# Chapter 6
# Final Remarks

## 6.1 Conclusion

POP is a medical condition related to the weakening of the pelvic muscles and ligaments with high levels of prevalence among women, especially of advanced age. Once these structures are responsible for the support and the well-functioning of the organs inside the pelvic cavity, their impairment induces complications that compromise the patients' health. When the damage of the USLs and CLs reaches a severe degree, the organs may be displaced leading to pelvic prolapse.

The intricacy of the pelvic region and its consequent demand for complex analyses and treatments is the reason for the associated techniques having received constant improvements over the past years. Nevertheless, these approaches will still require further technical investigation that, along with medical counselling, might deliver more adequate solutions. A clear conclusion to take from the current work is how crucial the stability of the pelvic region is for women of all ages. Currently, the main hope lies on surgical implants and their active optimization, aiming at a smoother engagement with host biological tissues, as well as at more efficient structural performances. Past solutions have not shown perfect results on these matters and were eventually banned from commercialization and implementation, for the sake of the patients' safety

The current work aimed at modelling mesh implants in ABAQUS® software – starting with the filaments that compose them – and understanding the mechanical properties of PCL – a 3D printed biodegradable polymer. Making use of existent experimental data from uniaxial tensile tests, it was possible to simulate filaments' performance as a function of their section area – two diameters were tested. Moreover, once the main goal was to identify the constitutive model that best reproduced the experimental results, different models were applied in order to reach a conclusion on this concern. Imposing boundary displacements on one end of each filament – 6.27 and 10% of the total length for the 160 and 240 micrometres diameter filaments, respectively – the stress values would answer this question. It was clear that, for a single filament, the linear elastic model offered the most accurate results, followed by the hyperelastic Yeoh and Neo-Hookean models. This perception enabled the modelling

of different mesh geometries for which experimental data was also available.

As the work moved forward, the meshes were also replicated and given modeled according to the constitutive law that had been settled as most appropriate during the filaments' simulations. All the models were exclusively tested inside the comfort zone of deformation - applying a displacement of 13% of the total length - since this is the range were the a linear elastic behavior was witnessed during the experimental uniaxial tensile tests. From here it was then possible to conclude that different geometries show different stress-strain responses, and that the thickness of the meshes also plays an important role on this matter. The cross-shaped geometries tend to be better represented through the linear elastic model than the square-shaped ones. After comparing the stress-strain curves obtained from the simulations, it is clear that the meshes built with the 160 micrometres diameter filaments are the best option to match the vaginal tissue curve up to a 6% elongation and that the meshes built with the 240 micrometres diameter filaments and the Restorelle® commercial mesh show similar behaviours inside the comfort zone. The prevalence of the influence of the geometry, as well as of the thickness, enables a promising understanding for eventually finding solutions that better address POP.

## 6.2 Future Work

Aiming at further developments on the subject studied in the current work, the author sees geometry manipulation and optimization as the main course to follow - changes and improvements on this regard will allow control over the stiffness of the meshes. Once enough computational models are developed for the meshes, the optimization of sectional areas might also be possible, enabling the production of prototypes with variable thicknesses. Creating databases for this instances shall be the first step to achieve this extra degrees of freedom in mesh design. For the curious reader to investigate further, an interesting fact is the resemblance between the stress-strain curves of the vaginal tissue and the ones associated with spiral shaped spider webs.

Another important topic shall be investigating different materials, capable of providing enough elasticity to operate with bigger deformation values. The current work only addressed the comfort zone but a functional surgical implant is supposed to be capable of responding beyond that limit.

As a final remark, the convergence between medical and technical knowledge, together with how patient report the sensation induced by the implants, will be crucial for POP to be pacifically treated in the future. The need for personalized approaches, eventually based on MRI's shall bring for efficient solutions. A better general understanding of the pelvic muscles and ligaments is also strongly related to these improvements.

# Bibliography


[1] C. A. Garbe et al., "Estudo biomecânico para reabilitação do ouvido médio humano," 2010.

[2] A. Partin, C. Peters, L. Kavoussi, and R. Dmochowski, "Campbell walsh wein urology."

[3] P. S. Shoureshi, W. Lee, K. C. Kobashi, and K. P. Sajadi, "Media coverage of the 2019 united states food and drug administration ordered withdrawal of vaginal mesh products for pelvic organ prolapse," International Urogynecology Journal, vol. 32, no. 2, pp. 375–379, 2021.

[4] E. Løwenstein, B. Ottesen, and H. Gimbel, "Incidence and lifetime risk of pelvic organ prolapse surgery in denmark from 1977 to 2009," International urogynecology journal, vol. 26, no. 1, pp. 49–55, 2015.

[5] M. N. B. d. Cunha, R. Rynkevic, M. E. T. d. Silva, A. F. Moreira da Silva Brandao, J. L. Alves, and A. A. Fernandes, "Melt electrospinning writing of mesh implants for pelvic organ prolapse repair," 3D Printing and Additive Manufacturing, 2021.

[6] D. Chow and L. V. Rodríguez, "Epidemiology and prevalence of pelvic organ prolapse," Current opinion in urology, vol. 23, no. 4, pp. 293–298, 2013.

[7] J. E. Jelovsek, C. Maher, and M. D. Barber, "Pelvic organ prolapse," The Lancet, vol. 369, no. 9566, pp. 1027–1038, 2007.

[8] M. E. T. da Silva, "Evaluating the mechanical properties of biological soft tissues using inverse methods: application to the pelvic floor muscles," 2017.

[9] S. Herschorn, "Female pelvic floor anatomy: the pelvic floor, supporting structures, and pelvic organs," Reviews in urology, vol. 6, no. Suppl 5, p. S2, 2004.

[10] P. J. Bazira, "Clinically applied anatomy of the pelvis," Surgery (Oxford), 2021.

[11] L. Keith, A. Moore, and A. Agur, Clinically oriented anatomy, vol. 291. Lippincott Williams & Wilkins, 2006.

[12] C. Iglesia and K. R. Smithling, "Pelvic organ prolapse," American family physician, vol. 96, no. 3, pp. 179–185, 2017.

[13] H. Pang, L. Zhang, S. Han, Z. Li, J. Gong, Q. Liu, X. Liu, J. Wang, Z. Xia, J. Lang, et al., "A nationwide population-based survey on the prevalence and risk factors of symptomatic pelvic organ prolapse in adult women in china–a pelvic organ prolapse quantification system-based study," BJOG: An International Journal of Obstetrics & Gynaecology, vol. 128, no. 8, pp. 1313–1323, 2021.

[14] I. Diez-Itza, I. Aizpitarte, and A. Becerro, "Risk factors for the recurrence of pelvic organ prolapse after vaginal surgery: a review at 5 years after surgery," International Urogynecology Journal, vol. 18, no. 11, pp. 1317–1324, 2007.

[15] K. Bø, F. Lilleås, T. Talseth, and H. Hedland, "Dynamic mri of the pelvic floor muscles in an upright sitting position," Neurourology and Urodynamics: Official Journal of the International Continence Society, vol. 20, no. 2, pp. 167–174, 2001.

[16] C. Persu, C. Chapple, V. Cauni, S. Gutue, and P. Geavlete, "Pelvic organ prolapse quantification system (pop–q)–a new era in pelvic prolapse staging," Journal of medicine and life, vol. 4, no. 1, p. 75, 2011.

[17] R. C. Bump, A. Mattiasson, K. Bø, L. P. Brubaker, J. O. DeLancey, P. Klarskov, B. L. Shull, and A. R. Smith, "The standardization of terminology of female pelvic organ prolapse and pelvic floor dysfunction," American journal of obstetrics and gynecology, vol. 175, no. 1, pp. 10–17, 1996.

[18] S. Swift, P. Woodman, A. O'Boyle, M. Kahn, M. Valley, D. Bland, W. Wang, and J. Schaffer, "Pelvic organ support study (posst): the distribution, clinical definition, and epidemiologic condition of pelvic organ support defects," American journal of obstetrics and gynecology, vol. 192, no. 3, pp. 795–806, 2005.

[19] S. L. Hendrix, A. Clark, I. Nygaard, A. Aragaki, V. Barnabei, and A. McTiernan, "Pelvic organ prolapse in the women's health initiative: gravity and gravidity," American journal of obstetrics and gynecology, vol. 186, no. 6, pp. 1160–1166, 2002.

[20] A. L. Olsen, V. J. Smith, J. O. Bergstrom, J. C. Colling, and A. L. Clark, "Epidemiology of surgically managed pelvic organ prolapse and urinary incontinence," Obstetrics & Gynecology, vol. 89, no. 4, pp. 501–506, 1997.

[21] M. Abdel-Fattah, A. Familusi, S. Fielding, J. Ford, and S. Bhattacharya, "Primary and repeat surgical treatment for female pelvic organ prolapse and incontinence in parous women in the uk: a register linkage study," BMJ open, vol. 1, no. 2, p. e000206, 2011.

[22] J. O. DeLancey, L. K. Low, J. M. Miller, D. A. Patel, and J. A. Tumbarello, "Graphic integration of causal factors of pelvic floor disorders: an integrated life span model," American journal of obstetrics and gynecology, vol. 199, no. 6, pp. 610–e1, 2008.

[23] W. R. Barone, P. A. Moalli, and S. D. Abramowitch, "Textile properties of synthetic prolapse mesh in response to uniaxial loading," American journal of obstetrics and gynecology, vol. 215, no. 3, pp. 326–e1, 2016.

[24] M. . Gyhagen, M. Bullarbo, T. Nielsen, and I. Milsom, "Prevalence and risk factors for pelvic organ prolapse 20 years after childbirth: a national cohort study in singleton primiparae after vaginal or caesarean delivery," BJOG: An International Journal of Obstetrics & Gynaecology, vol. 120, no. 2, pp. 152–160, 2013.

[25] S. Hagen and D. Stark, "Conservative prevention and management of pelvic organ prolapse in women," Cochrane Database of Systematic Reviews, no. 12, 2011.

[26] S. C. de Albuquerque Coelho, E. B. de Castro, and C. R. T. Juliato, "Female pelvic organ prolapse using pessaries: systematic review," International Urogynecology Journal, vol. 27, no. 12, pp. 1797–1803, 2016.

[27] M. P. FitzGerald, H. E. Richter, S. Siddique, P. Thompson, and H. Zyczynski, "Colpocleisis: a review," International Urogynecology Journal, vol. 17, no. 3, pp. 261–271, 2006.

[28] T. Mascarenhas, "Disfunções do pavimento pélvico: incontinência urinária e prolapso dos órgãos pélvicos," EDITORS. Manual de Ginecologia. Lisboa (PT): Permanyer, vol. 2, pp. 283–98, 2011.

[29] M. Silva, J. Bessa, M. Parente, T. Mascarenhas, R. N. Jorge, and A. Fernandes, "Effect of mesh anchoring technique in uterine prolapse repair surgery: A finite element analysis," Journal of Biomechanics, vol. 127, p. 110649, 2021.

[30] S. Misra and V. Tyagi, "Management of complications of mesh surgery," Obstetrics, Gynaecology & Reproductive Medicine, vol. 29, no. 11, pp. 314–319, 2019.

[31] E. Holt, "Us fda rules manufacturers to stop selling mesh devices," The Lancet, vol. 393, no. 10182, p. 1686, 2019.

[32] N. Ng-Stollmann, C. Fünfgeld, B. Gabriel, and A. Niesel, "The international discussion and the new regulations concerning transvaginal mesh implants in pelvic organ prolapse surgery," International urogynecology journal, vol. 31, no. 10, pp. 1997–2002, 2020.

[33] T. D. Brown, P. D. Dalton, and D. W. Hutmacher, "Melt electrospinning today: An opportune time for an emerging polymer process," Progress in Polymer Science, vol. 56, pp. 116–166, 2016.

[34] M. L. Muerza-Cascante, D. Haylock, D. W. Hutmacher, and P. D. Dalton, "Melt electrospinning and its technologization in tissue engineering," Tissue Engineering Part B: Reviews, vol. 21, no. 2, pp. 187–202, 2015.

[35] L. W. McKeen, Permeability properties of plastics and elastomers. William Andrew, 2016.

[36] G. A. Holzapfel, "Nonlinear solid mechanics: a continuum approach for engineering science," Meccanica, vol. 37, no. 4, pp. 489–490, 2002.

[37] N.-H. Kim, "Finite element analysis for nonlinear elastic systems," in Introduction to Nonlinear Finite Element Analysis, pp. 141–239, Springer, 2015.

[38] J. Bonet and R. Wood, "Nonlinear continuum mechanics for finite element analysis, 2nd edn cambridge university press. doi: 10.1017," CBO9780511755446.[CrossRef][Google Scholar], 2008.

[39] J. Bonet, A. J. Gil, and R. D. Wood, Nonlinear solid mechanics for finite element analysis: statics. Cambridge University Press, 2016.

[40] A. F. Bower, Applied mechanics of solids. CRC press, 2009.

[41] A. E. Tekkaya and C. Soyarslan, Finite Element Method, pp. 508–514. Berlin, Heidelberg: Springer Berlin Heidelberg, 2014.

[42] D. Hibbit, B. Karlsson, and P. Sorenson, "Abaqus analysis user's manual, version 6.5," Hibbit, Karlsson & Sorenson Inc., USA, 2004.

[43] J. N. M. Bessa, "Modelação numérica de redes sintéticas para correção de prolapso uterino," 2020.

[44] S. Eshraghi and S. Das, "Mechanical and microstructural properties of polycaprolactone scaffolds with 1-d, 2-d, and 3-d orthogonally oriented porous architectures produced by selective laser sintering," Acta biomaterialia, vol. 6, no. 7, p. 2467, 2010.